

SPECTRAL ESTIMATION OF PLASMA FLUCTUATIONS II: NONSTATIONARY ANALYSIS OF ELM SPECTRA

Kurt S. Riedel*, Alexander Sidorenko*,
Norton Bretz†, and David J. Thomson+

* Courant Institute of Mathematical Sciences,
New York University, New York, New York 10012-1185

† Princeton Plasma Physics Laboratory, Princeton, NJ 08544-0451

+ AT&T Bell Laboratories, Murray Hill, NJ 07974-0636

Abstract

Several analysis methods for nonstationary fluctuations are described and applied to the edge localized mode (ELM) instabilities of limiter H-mode plasmas. The microwave scattering diagnostic observes poloidal k_θ values of 3.3 cm^{-1} , averaged over a 20 cm region at the plasma edge. A short autoregressive filter enhances the nonstationary component of the plasma fluctuations by removing much of the background level of stationary fluctuations. Between ELMs, the spectrum predominantly consists of broad-banded 300-700 kHz fluctuations propagating in the electron diamagnetic drift direction, indicating the presence of a negative electric field near the plasma edge. The time-frequency spectrogram is computed with the multiple taper technique. By using the singular value decomposition of the spectrogram, it is shown that the spectrum during the ELM is broader and more symmetric than that of the stationary spectrum. The ELM period and the evolution of the spectrum between ELMs varies from discharge to discharge. For the discharge under consideration which has distinct ELMs with a 1 msec period, the spectrum has a maximum in the electron drift direction which relaxes to a near constant value in the first half millisecond after the end of the ELM and then grows slowly. In contrast, the level of the fluctuations in the ion drift direction increases exponentially by a factor of eight in the five milliseconds after the ELM. High frequency precursors are found which occur one millisecond before the ELMs and propagate in the ion drift direction. These precursors are very short ($\sim 10 \mu\text{secs}$), coherent bursts, and they predict the occurrence of an ELM with a high success rate. A second detector, measuring fluctuations 20 cm from the plasma edge with k_θ values of 8.5 cm^{-1} , shows no precursor activity. The spectra in the ion drift direction are very similar on both detectors, while the “electron” spectrum level is significantly larger on this second detector.

PACS 52.35, 52.55, 52.70, 06., 2.50

I. Introduction

Edge localized modes (ELMs) occur in the H-mode phase^{1,2} of a tokamak discharge and are usually associated with periodic loss of confinement and transient deposition of heat on the divertor/limiter. A variety of different types of ELMs have been observed (and ELM precursors)¹⁻⁷, and there remains no widespread consensus on the nature and causes of ELMs. Therefore, it is desirable to understand the physical characteristics of ELMs and if possible to predict their occurrence.

In one class of ELM discharges^{1,5,6}, a magnetohydrodynamic (MHD) precursor is seen prior to the ELM. When the precursor lasts for many sampling times and consists of a single mode, straightforward analysis is adequate to resolve the basic features of the ELM precursor. Another class of precursors²⁻⁵, consisting of a transient burst of high frequency fluctuations, has also been observed. For these short lived bursts, the choice of analysis methods can noticeably enhance the resolution of the transient events.

In this article, we describe a number of advanced signal processing techniques and apply these methods to a limiter H-mode discharge from the tokamak fusion test reactor (TFTR)^{2,7,8}. Our goal is to show how these methods give high resolution estimates of transient plasma fluctuations. In a previous article⁹, we describe advanced spectral analysis methods which give highly accurate spectral estimates for relative short time series. For the transient ELM precursors, the typical data length is 100 points so that high resolution estimates are particularly important.

We examine the evolution of the spectrum between ELMs. The spectral density fluctuates strongly on the millisecond time scale. This indicates that there are only a very small number of waves present in a given frequency range at one time. When the spectrum is averaged over a number of milliseconds, the fluctuations can be treated as a stationary process.

The time period between ELMs and the spectral evolution between ELMs varies appreciably between discharges. We consider a particular TFTR discharge, # 49035, which has particularly well defined ELMs. We caution that other TFTR discharges sometimes have distinctly different behavior and that no single pattern can describe the ELM behavior in all discharges.

Our results confirm the findings of Kaye et al.³ and McGuire et al.⁴ that one or more short bursts of high frequency fluctuations precede the ELM by a fraction of a millisecond. Our findings give a more precise characterization of the TFTR ELM precursors: the precursor bursts occur in the 500 kHz range propagating in the ion drift direction, and therefore have a spectral density which is distinctly different from

both the stationary spectrum between ELMs and the ELM spectrum itself. Our sampling rate is ten times faster than that in Ref. 3; thus it is understandable that we observe precursors with one tenth the duration as Kaye et al³. We often use the terms “electron” spectrum and “ion” spectrum to denote the poloidal direction of propagation in the electron and ion diamagnetic drift directions respectively.

After the ELM, the intensity of the spectrum in the electron drift direction grows by 50–80% during the first half millisecond after the end of an ELM. After the half millisecond, the intensity of the electron drift spectrum saturates at a more or less constant value. In contrast, *the intensity of the spectrum in the ion drift direction increases exponentially between ELMs. During the 5-6 milliseconds between ELMs, this “ion” spectrum grows by a factor of eight.* When this “ion” spectrum grows more slowly, the onset of the ELM is delayed. Thus, in this particular discharge, the ELM onset appears correlated with the “ion” spectrum reaching a critical level.

In Section II, we describe the TFTR H-mode microwave scattering data set^{10–12} which we use as an example. In Section III, we review autoregressive filters^{13,14} and show how these filters highlight nonstationary phenomena. We consider time-frequency representations of evolutionary spectra^{15,16} in the next three sections. In Section IV, we compute the singular value decomposition of the time-frequency distribution to isolate the spectrum during the ELMs. In Section V, we examine the evolution of the spectral density between ELMs. In Section VI, we use a high resolution, prewhitened, multitapered evolutionary spectral estimate to examine high frequency precursors to the ELMs.

II. Stationary analysis of the TFTR ELM data set

a) Microwave scattering data set

The TFTR microwave transmitter launches a 60 GHz plasma wave linearly polarized in the extraordinary mode below the electron cyclotron frequency^{10–11} at 112 GHz. The 60 GHz extraordinary mode plasma wave propagates in the poloidal plane through the plasma to the edge, where plasma density fluctuations scatter the incoming wave. Figure 1 displays a ray tracing calculation of the extraordinary mode wave path. The center of the beam path is the central curve while the outer curves mark the beam $\frac{1}{e}$ power half-width of 5.0 cm. The scattered wave is measured by two detectors located near the bottom of the vacuum vessel. A third detector at the top of the vessel, known as detector #1, measures backscattered power at $|\vec{k}_{scat}| \simeq 20 \text{ cm}^{-1}$, and is not used in this article.

We examine the fluctuation spectrum of TFTR discharge #49035 as measured by the microwave scattering diagnostic^{10–12}. The detected signal is down-shifted from 60 GHz to 1 MHz using standard intermediate frequency (IF) techniques. The time series begins 4.2 sec into the discharge, and is totally contained in the H-mode phase. Our data consist of 524,288 time samples with a uniform sampling rate of 5 MHz over the time interval. Thus, the fluctuations are recorded over a tenth of a second time interval. The data has been band-pass filtered with an anti-aliasing filter with a low-pass filter half-width of 2.5 MHz.

For TFTR discharge #49035, the plasma parameters are the toroidal magnetic field: $B_t = 4.0$ Tesla; the edge q , $q_a = 5.7$; the total current, $I_p = 0.9$ MA; the line average density, $\bar{n}_e = 2.5 \times 10^{13}$ cm⁻³; and the absorbed power, $P_{NBI} = 13$ MW. The central electron temperature is approximately 6 keV and the central ion temperature is approximately 21 keV. In the scattering volume, the local plasma parameters are $\rho_i = 0.16$ cm, $\rho_S \simeq \rho_i \sqrt{T_e/T_i} = 0.09$ cm.

We concentrate on detector #3, which measures fluctuations averaged over a 20 cm region at the plasma edge. Figure 1a displays the geometry of the transmitted extraordinary mode and the receiver antenna pattern. The three curves emerging from the bottom right are the center of the detector line of sight and its inner and outer $\frac{1}{e}$ power sensitivity. The ellipses denote the product of the transmitter power profile and the receiver antenna profile. Detector #3 measures $|\vec{k}_{scat} - \vec{k}_{inc}| \simeq 3.3$ cm⁻¹ and \vec{k} is parallel to the poloidal magnetic field at $\frac{r}{a} \simeq 1.0 \pm 0.1$.

Detector #2 measures fluctuations somewhat farther in the plasma interior, at $\frac{r}{a} \simeq 0.75 \pm 0.1$ with $|\vec{k}_{scat} - \vec{k}_{inc}| \simeq 8.5$ cm⁻¹. Figure 1b gives the corresponding line of sight information for detector #2. Unless otherwise specified, our analysis is based on detector #3, and detector #2 will be used for comparison. Unfortunately, we cannot determine whether the signal differences from detector #2 to #3 are due to detector #2 measuring smaller wavelength turbulence or due to the scattering volume for detector #2 being located farther in the interior of the plasma. ELM activity is not observed when the center of the scattering volume is located inside $\frac{r}{a} \simeq 0.5$.

These strongly beam-heated discharges are rotating toroidally with a velocity profile which is peaked on axis with $v_\phi(r = 0) \sim 10^6 - 10^7$ cm/sec. At the edge, the toroidal rotation is typically very small, $v_\phi < 3 \times 10^5$ cm/sec. Because the fluctuations are primarily aligned perpendicular to the total magnetic field, the observed poloidal Doppler shift is proportional to $\Delta\omega \simeq k_\theta v_\phi(r) \frac{B_\theta}{B_\phi}$. Thus, only spectral shifts of less than 20 kHz may be due to toroidal fluid motion². The ion and electron drift frequencies are approximately 50 kHz at $\frac{r}{a} \simeq 0.9$ for $\tilde{k}_\theta \simeq 3.3$ cm⁻¹. Detailed profile information in the region $0.9 \leq \frac{r}{a} \simeq 1.0$ is not available, however.

b) Exploratory analysis

We begin by computing the spectrum using the multiple spectral window analysis as described in Refs. 9, 17-19. We use 20 orthogonal tapers and then kernel smooth the estimate over a 20 kHz frequency bandwidth. In assuming the plasma fluctuations are stationary, we are averaging the fluctuation spectrum over the short ELM bursts and the long quasistationary times between ELMs. Figure 2 displays this “composite” spectrum which we compute using the smoothed multitaper method^{9,17,19}. The solid curve is the estimated spectrum from detector #3 and the dashed curve is from detector #2.

On detector #3, a frequency shift greater than 1 MHz represents fluctuations which are traveling poloidally in the electron drift direction in the laboratory frame. Frequency shifts less than 1 MHz correspond to fluctuations moving in the ion drift direction in the laboratory frame. Detector #2 measures k_θ fluctuations with the \tilde{k}_θ direction reversed in comparison with that of detector #3, and therefore electron drift frequencies are reversed with respect to 1 MHz on detector #2. To compensate for this reversal of \tilde{k}_θ in detector #2, we have reflected the frequencies about the 1 MHz line: $f \rightarrow 1 \text{ MHz} - f$.

The spectral peak near 1 MHz is partially coherent. The broadening of the 1 MHz peak is believed to be due to intense edge fluctuations^{9,11,12} at low k , $k_\perp \sim 0.1 \text{ cm}^{-1}$. The detector sensitivity to these low k fluctuations is weak, but the edge fluctuation intensity is sufficiently large that broadening is appreciable. The broadening of the 1 MHz line on detector #3 is larger than that of detector #2 because detector #3 measures fluctuations much closer to the plasma edge.

The spectrum is asymmetric with a larger spectral density on the high frequency/electron drift side, as is typical of H-mode discharges². There is a plateau in the spectral density from 1300 kHz to 1500 kHz. A frequency shift of 300 kHz at $k_\perp \simeq 3.3 \text{ cm}^{-1}$ corresponds to a fluid velocity of $\tilde{v}_\theta \simeq \frac{2\pi\Delta f}{k_\theta} \sim 6 \times 10^5 \text{ cm/sec}$. The edge toroidal rotation velocity is measured by the CHERS diagnostic^{2,8}, and is at most $\frac{B_\theta}{B_\phi} \times 3 \times 10^5 \text{ cm/sec} \simeq 3 \times 10^4 \text{ cm/sec}$. Thus, the toroidal rotation is not responsible for the frequency shift. The poloidal fluid rotation velocity is not measured, and can account for an unknown but significant fraction of the frequency shift.

The other possible explanation for the asymmetric broadening of the spectrum is the presence of plasma fluctuations which are propagating in the electron drift direction with a frequency range of 300-700 kHz. These fluctuations have frequencies five to ten times larger than the electron diamagnetic frequency. We are unaware of

any plasma instabilities with frequencies in this range. Thus, we believe the most likely cause of the frequency shift is the presence of a strong poloidal electric field, leading to strong poloidal fluid motion. We also measure fluctuations in the ion drift direction in the 500 kHz range. One explanation is that the gradient in the poloidal electric field is sufficiently strong that both the ion and electron frequency shifts are caused by the poloidal electric field which is changing signs within the scattering volume. In DIII-D^{5,20,21}, H-mode electric fields are observed to be negative near the edge scrape-off layer and to become positive in the interior.

In discharges such as #49035, we primarily measure the poloidal component of the wave vector. In other discharges where the fluctuations are primarily measured in the radial direction, we find the frequency shift is much less. This supports our belief that the poloidal electric field is primarily responsible for the frequency shift.

In Figure 2, the spectrum in the ion drift direction *decays exponentially in frequency with the same rate in both detectors*. To normalize the amplitudes, we have multiplied the spectrum of detector #2 by a factor of ten. We have chosen this normalization such that the amplitudes of the two detectors are the same for the frequencies where the spectrum of detector #3 begins to broaden rapidly. This normalization is natural because these frequencies constitute the beginning of the true scattered signal. With this normalization, the “ion” spectrum in both detectors has the same amplitude while the electron amplitude is three times larger. Since our normalization of detector #2 is somewhat arbitrary, the precise ratio is also arbitrary. Nevertheless, the electron turbulence is stronger on detector #2, and thus the electron turbulence is stronger at $\frac{r}{a} \simeq 0.75$ than at $\frac{r}{a} \simeq 1.0$, or the electron turbulence is stronger for $\tilde{k}_\theta \simeq 3.3 \text{ cm}^{-1}$ than for $\tilde{k}_\theta \simeq 8.5 \text{ cm}^{-1}$.

Figure 3a displays the 12 millisecond data segment from $t = 2$ msec to $t = 14$ msec. The ELMs occur at $t = 6.07$ and 13.19 msec. We will show that characteristically, ELM precursor bursts are centered in the 250 – 650 kHz range roughly 1 msec prior to the ELM. Two of these precursor bursts in the 250 – 650 kHz range occur at $t = 5.186$ and 12.734 msec. But, it is very difficult to identify the 250 – 650 kHz bursts in the raw data.

The ELMs appear to consist of a series of distinct bursts, and resemble a sinusoid which is modulated at high frequency. We have tried unsuccessfully to develop a joint time-frequency representation of the ELM burst.

III. Autoregressive filters to enhance nonstationary events

In this section, we assume that the measured time series, $\{x_i\}$, is related to an underlying basic time series, $\{z_i\}$, through an autoregressive (AR) process^{13,14} of order p :

$$x_t = \sum_{i=1}^p \alpha_i^{(p)} x_{t-i} + z_t . \quad (1)$$

$\{z_i\}$ is called the innovation sequence because it is usually assumed to be a series independent random perturbations. The autoregressive model introduces time correlation into the measured time series through the autoregressive lag parameters, $\alpha_i^{(p)}$. We denote an autoregressive filter of length p by $\text{AR}(p)$.

Several different numerical methods for determining the autoregressive lag parameters, $\alpha_i^{(p)}$, are given in Refs. 13-14. We estimate the autoregressive parameters by solving the Yule-Walker equations, i.e. minimize the residual sum of squares:

$$\hat{\sigma}_z^2 = \frac{1}{N-p} \sum_{t=p}^N \left(x_t - \sum_{i=1}^p \alpha_i^{(p)} x_{t-i} \right)^2 . \quad (2)$$

The main point of this section is that *the autoregressive filter appreciably enhances the nonstationary bursts in the data because the filter removes the stationary part of the signal*. Figure 3a displays the raw data and Fig. 3b plots the residuals, $\{z_i\}$, of the autoregressive filter.

In Figure 3b, the ELM amplitude is enhanced relative to the background level because the ELM spectrum is broader than the ambient spectrum. The two precursor bursts in the 250–650 kHz range, at $t = 5.186$ and 12.734 msecs, have been noticeably enhanced relative to the raw data of Fig. 3a. The large residuals in Fig. 3b last for roughly 60 data points, which corresponds to 11 μsec . A third precursor in the 250 – 650 kHz range, at $t = 5.56$ msecs, is less visible in the AR residual plot and can only be seen in the time-frequency plots of Sec. VI.

In Figure 3a, there are two large non-ELM bursts, at $t = 2.44$ and 3.01 msecs, which are centered in the 1 MHz frequency range. Most of the other fluctuation bursts are also due to changes in the 1 MHz frequency range (shown in Sec. VI). These 1 MHz features are greatly reduced in Fig. 3b due to the AR filter.

As a second example to illustrate the power of the AR filter to emphasize nonstationary bursts, we consider the Ohmic sawtooth TFTR discharge # 50616 which we studied in Ref. 9. For this discharge, the microwave scattering volume is centered at $\frac{r}{a} = 0.3$ and $k_\theta = 4 \text{ cm}^{-1}$. Figure 4a displays the 65,535 point raw data. The sawtooth oscillation at 3.86 msec is barely visible. The blip at 9.12 msec is an unknown and unrelated event. Fig. 4b plots the residuals of the autoregressive filter which nearly removes the 1 MHz peak. The sawtooth is easily discernable in the filtered data in contrast to the raw data.

The variance of the raw data in Fig. 4a appears to be increasing in time, thereby calling into question the assumption of stationarity. Figure 4b shows that the filtered data has no temporal increase in the variance. Thus the increasing variance of the raw data is associated with the 1 MHz IF of the receiver and not with the broad-banded plasma fluctuations^{11,12}. The changing amplitude of the 1 MHz peak occurs due to phase changes between the scattered signal and the local oscillator of the detection circuit and is not directly related to changes in the plasma fluctuations.

The autoregressive model may also be used to detect and correct statistical outliers. We compare the measured data with the predicted value given by the AR model. When the residual error is many standard deviations large, we mark/plot the outliers for further scrutiny. In robust spectral estimation^{22,23}, severe statistical outliers are replaced by their fitted values. In robustifying the data, we focus on the stationary spectrum and discard the transient burst associated with the ELMs and precursors. Since we are primarily interested in these transient phenomena, we *do not robustify* the data.

When both processes are stationary, the spectra of the measured and innovation processes, $\{x\}$ and $\{z\}$, are related by

$$S_x(f) = \frac{S_z(f)}{\left|1 - \sum_{k=1}^p \alpha_k^{(p)} e^{-2\pi i k f}\right|^2} = |\Gamma(f)|^2 S_z(f) , \quad (3)$$

where the spectral transfer function, $\Gamma(f)$, is defined by Eq. (3). In AR spectral analysis, we assume that the autoregressive filter has removed all of the time correlation and that $\{z_i\}$ are independent identically distributed random variables with variance, σ_z^2 , estimated by Eq. (2). The resulting AR spectral estimate is given by Eq. (3) with $S_z(f) = \hat{\sigma}_z^2$.

Thus, the AR spectral estimate is a rational approximation to the actual spectral density function $S(f)$. This type of low order spectral approximation tends to describe the bulk characteristics of simple spectra well, but has difficulty resolving the fine features of the spectrum. Figure 5 shows AR(10) and AR(20) fits to the spectrum. The AR fitted spectra have difficulty fitting the spectral plateau between 1450-1600 kHz. By AR(20), the reduction in the root mean squared error has virtually saturated as a function of the filter order. *Using the the autoregressive filter accentuates the transient bursts because it applies the filter, $\Gamma(f)^{-1}$, to remove the ambient spectrum, especially the 1 MHz peak, and therefore accentuates the frequency components which are only weakly present in the ambient spectrum.*

Spectral prewhitening^{13,14} was developed by J. Tukey to reduce the spectral variation in the analyzed time series. Prewhitening uses the AR model as an initial

filter and then uses local, Fourier-based methods, such as the smoothed periodogram or multiple taper analysis to estimate the spectrum of the residual process, $\{z\}$. Prewhitening implicitly assumes that the autoregressive parameters, $\alpha_i^{(p)}$, are independent of the measured and residual processes. In our precursor analysis in Sec. VI, we use a prewhitening filter prior to computing the time-frequency distribution.

IV. Nonstationary plasma fluctuations during the ELMs

When the plasma fluctuations are stationary stochastic processes, we can identify the time autocovariance of the fluctuations with the Fourier transform of the spectral density $S(f)$. In Ref. 9, we compare methods of estimating the spectral density for stationary plasma fluctuations. When the spectral density is changing slowly in time, the natural generalization is that of Karhunen processes^{14–16}:

$$x_t = \int_{-1/2}^{1/2} A(f, t) e^{ift} dZ(f) , \quad (4)$$

where $dZ(f)$ is a white noise process with independent spectral increments. When $A(f, t)$ evolves slowly with respect to the sampling rate, we can interpret x_t as an approximately stationary process. The evolutionary spectrum, $S(f, t) = |A(f, t)|^2$, then corresponds to the instantaneous value of the spectral density.

To estimate the evolutionary spectrum, first we compute the local Fourier transform, $y(f, t)$, of x_t using a sliding tapered (or multitapered) time window, and the one point spectral estimate is $\hat{S}(f, t) = |y(f, t)|^2$, which we evaluate on a time-frequency grid. When the sampling rate is much larger than the characteristic time scale, we can improve on these point estimates of the evolutionary spectrum by smoothing the spectral density in time and frequency¹⁶. However, we are not in this limit due to the burstlike nature of the ELMs and precursors.

A good model for these plasma fluctuations is that the fluctuations consist of a stationary component and a transient bursting component:

$$S(f, t) = \bar{S}(f) + A_e(t)S_e(f) + \tilde{S}(f, t) , \quad (5)$$

where the subscript e denotes “ELM”, and $\tilde{S}(f, t)$ is the residual transient spectrum. To estimate $\bar{S}(f)$, $A_e(t)$, and $S_e(f)$, we begin by computing a multiple taper estimate of $S(f, t)$. To retain high time-frequency resolution, we use 1000-point segments with 8 tapers ($w \sim 20$ kHz). We subtract the mean values, $\bar{S}(f)$: $S(f, t) - \bar{S}(f)$, and then estimate $A_e(t)S_e(f)$ by computing the singular value decomposition of

$$\hat{S}(f, t) - \hat{\bar{S}}(f) = \sum_k \lambda_k A_k(t) h_k(f) . \quad (6)$$

The singular value decomposition divides the spectrum into its fundamental components²⁴. Neither $A_k(t)$ nor $h_k(f)$ need be positive. We equate $A_e(t)h_e(f)$ with $\lambda_1 A_1(t)S_1(f)$.

In practice, we find that the quasi-coherent part of the 1 MHz peak has a different time evolution than the rest of the spectrum. To remove the effect of the IF frequency, we band limit the signal to exclude the 1 MHz peak ± 40 kHz prior to computing the singular value decomposition. Figure 6 displays the mean spectral estimate, where we have used 1000 data points corresponding to a 0.4 msec time interval with 8 tapers.

The mean spectrum is similar to, but broader than, the multitaper estimate in Fig. 2. The broadening occurs because we have lowered the frequency resolution to increase the time resolution. Figure 7 presents the first singular time vector, $A_1(t)$, which corresponds to the ELM bursts. The actual rise time of the ELMs is much sharper than that displayed in Figure 7. As we increase the time resolution, the rise time of the ELMs decreases with the time window length. Therefore the rise time is not resolved.

Figure 8 displays the corresponding first singular frequency vector, which is broader and more symmetric than the mean spectrum. The broader and more symmetric spectrum was originally observed in Ref. 12. However, the time-frequency singular value decomposition allows us to quantify the spectrum of a bursting event. $S_e(f)$, as estimated by the singular value decomposition, is essentially a time-weighted average of the spectra of the 14 ELMs with the weighting function given by $A_e(t)$.

Our singular value decomposition differs from that of Nardone²⁵ and Zohm et al.²⁶ because our two axes are time and frequency. In contrast, Refs. 25 & 26 have multiple measurement channels, and compute a singular value decomposition with time and space/mode number as the two axes.

V. Spectral evolution between ELMs

We now examine the temporal evolution of the spectral density between ELMs. We estimate the average growth rate as a function of frequency. Our results are strictly for discharge # 49035. Other discharges sometimes have significantly different spectral evolution, both quantitative and qualitative.

In our initial analysis, we computed the evolutionary spectrum as a sequence of spectral estimates. Due to the broad-banded nature of the plasma turbulence, we present only the total spectral energy in four 300 kHz bands versus time. By integrating in frequency, we reduce the variance of the estimate and display only the essential features of the data. We then estimate the growth rates of the spectrum

during the time after the end of an ELM.

To estimate $\bar{S}(\bar{f}, t) = \int_{\bar{f}-150\text{kHz}}^{\bar{f}+150\text{kHz}} S(f, t) df$, we estimate $S(f)$ on a 0.4 msec interval centered at t using a 100 taper estimate with $w = 150$ kHz. To further reduce the variance, we average $\log_{10}[\hat{S}(\bar{f}, t)]$ over all 14 quiescent periods. This averaging is necessary because the fluctuation level is highly variable, indicating that there are only one or two waves present at each frequency. We use the logarithm to reduce the influence of the outliers^{9,19}. This ELM averaging is reminiscent of sawtooth averaging in heat pulse propagation²⁷. In sawtooth averaging, the signal is averaged directly to reduce the noise while in ELM averaging, we average the log-spectrum to determine the spectrum of the noise.

Both the ELM duration and the length of time between ELMs varies from ELM to ELM. (See Table 1.) We find that the ELM duration is 1.2 ± 0.3 msec and that the quiescent time between ELMs is 6.1 ± 1.5 msec. After the 10th ELM, a large amplitude fluctuation burst occurs at $t = 79.15$ centered at 450 kHz. The length of time between the 10th and 11th ELM is considerably larger, 9.45 msec versus 5.8 msec. We believe that *this ion fluctuation burst indicates the release of some of the free energy which causes the ELM instability, and thereby delays the onset of the 11th ELM*. Excluding the time between the 10th and 11th ELM gives the typical time length between the end of the $(k - 1)$ th ELM and the beginning of the k th ELM to be 5.8 ± 1.1 msec.

Since the 14 quiescent periods vary in length, we need to standardize the intervals to all be of the same length prior to averaging the spectral estimates. With this standardization, the spectral evolution is clearly exponential. Figure 9 displays the mean value of $\log_{10}[\hat{S}](\bar{f}, t)$ after all quiescent periods are standardized to a length of 5.8 msec. The fluctuations in the electron drift direction increase rapidly in the first 0.5 msec after the ELM subsides. During the first half millisecond, the spectrum between 1500 & 1800 kHz grows by 50 percent and the spectrum between 1200 & 1500 kHz grows by 80 percent. During this time, the “ion” fluctuations actually decrease slightly.

To illustrate this spectral evolution, Fig. 10 plots the spectrum for three time slices, 0.1, 0.3, and 0.5 msec after the second ELM. The spectra were calculated with 8 tapers on 1000 data point segments, and have a frequency resolution of 20 kHz and a time resolution of 0.1 msec. The 1 MHz peak decreases in amplitude and in width. This narrowing of the 1 MHz line results in a reduction of the “ion” spectrum. The “electron” spectrum between 1600 and 1800 kHz is growing noticeably. In detector #2, the secondary maximum does not grow appreciably after the end of the ELM.

Figure 11 plots the corresponding spectral evolution for detector #2. The “ion”

spectrum hardly grows during the initial 0.8 msec after the ELM. The growth rates of the “electron” spectrum for detector #2 are roughly half of those of detector #3. But the initial phase of rapid growth lasts for nearly a full millisecond in detector #2 while the the rapid growth period in detector #3 is only half a millisecond long. Thus, the total growth of the “electron” spectrum in the two detectors is nearly the same. In the first millisecond, the “electron” spectrum grows by 50 % for f' in 1500 – 1800 kHz and by 100 % for f' in 1200 – 1500 kHz. (We continue to use $f' \equiv 1\text{MHz} - f$ for detector #2.) This suggests that the saturated amplitude is a weak function of the initial growth rate.

Estimating these initial growth rates, γ , with $S(t) \sim \exp(2\gamma t)$, we find that for detector #3, $\gamma = 0.5 \text{ msec}^{-1}$ for f in 1200 – 1500 kHz, and $\gamma = 0.37 \text{ msec}^{-1}$ for f in 1500 – 1800 kHz; for detector #2, $\gamma = 0.28 \text{ msec}^{-1}$ for f' in 1200 – 1500 kHz, and $\gamma = 0.24 \text{ msec}^{-1}$ for f' in 1500 – 1800 kHz. After this initial phase, the “electron” growth rates slow by a factor of three to five in detector #2 and by even less in detector #3.

During the 5.3 millisecond time period beginning 0.5 milliseconds after the end of the ELM, the level of the electron drift fluctuations grows slowly. In contrast, *the fluctuation level in the ion drift direction increases by a factor of five in the 500-800 kHz range and by a factor of eight in the 200-500 kHz range.* At the time of the onset of the ELM, the electron drift spectrum in 1200 & 1500 kHz range is roughly 50 % larger than the corresponding ion drift fluctuations. For detector # 2, the increase in the “ion” spectrum is less: a factor of $1.6 \times$ in the 500-800 kHz range and by nearly a factor of $2.2 \times$ in the 200-500 kHz range. The ratio of the total spectral energy in the ion drift direction to that of the energy in the electron drift direction is much less for detector #2 than for detector #3. This occurs because the electron is larger in detector #2 and the ion energy growth between ELM is less.

Beginning 0.5–1.0 millisecond after the ELM, the evolution of the “ion” spectrum enters into an exponential growth phase. During this later phase, we find $\gamma = 0.2 \text{ msec}^{-1}$ for f in 200 – 500 kHz, and $\gamma = 0.15 \text{ msec}^{-1}$ for f in 500 – 800 kHz for detector #3. For detector #2, $\gamma = 0.1 \text{ msec}^{-1}$ for f' in 200 – 500 kHz; for f' in 500 – 800 kHz, $\gamma = 0.17 \text{ msec}^{-1}$ for the time 0.3 to 1.3 msec after the ELM and $\gamma = 0.01 \text{ msec}^{-1}$ for later times. In summary, the “ion” growth rates are smaller by a factor of 2.5 – 3.0 times the initial “electron” growth rates. We stress that these growth rates vary appreciably from one discharge to another.

When the “ion” spectrum grows more slowly, the onset of the ELM is delayed. This suggests that the ELM is triggered when the “ion” spectrum near the edge reaches a critical level. By averaging $\log_{10}[\bar{S}(\bar{f}, t)]$ over 0.44 msec, we find that the critical levels

are $\log_{10}[\bar{S}(350\text{kHz}, t)] = 2.40 \pm 0.14$ and $\log_{10}[\bar{S}(650\text{kHz}, t)] = 3.45 \pm 0.14$. (See Table 2.) This corresponds to relative variations of 40% in the critical level. This variation seems large, but $\bar{S}(\bar{f}, t)$ increases by a factor of five to ten. Thus, the variance in the critical level is small relative to the total growth in the “ion” spectrum. The onset of the ELM need not be caused by the increased fluctuation level. Instead, both phenomena may be caused by the same destabilizing mechanism.

Standardizing the 14 interval lengths is successful because the final level of the ion fluctuations varies less than either the length of the quiescent interval or the exponential growth rate of the “ion” spectrum. If we believe that the interesting spectral evolution occurs immediately after the end of the ELMs, we should align the k th quiescent period at the end of $(k - 1)$ th ELM. If we believe that the interesting evolution occurs immediately prior to the start of the ELMs, we should align the k th quiescent period at the beginning of the k th ELM. We tried both of these normalizations; however, no clear pattern emerged and the ELM to ELM variance was larger than when interval lengths were standardized.

We estimate the variance of $\log_{10}[\hat{S}]$ using the empirical variance estimate from the 14 independent subsequences. We find that the empirical standard deviation, $\sigma(\bar{f}, t)$, of $\log_{10}[\hat{S}(\bar{f}, t)]$ varies little in time. For $\bar{f} = 1350$ and 1650 kHz, $\sigma(\bar{f}, t) \sim 0.1$, which corresponds to a relative variation of 25 %. For $\bar{f} = 650$ kHz, $\sigma(\bar{f}, t) \sim 0.15$, which corresponds to a relative variation of 40 % and for $\bar{f} = 350$ kHz, $\sigma(\bar{f}, t) \sim 0.19$, which corresponds to a relative variation of 55 %. These values of $\sigma(\bar{f}, t)$ are for detector #3. This variation is small relative to the total increase in the ion fluctuations over the 6 milliseconds. Furthermore, the variance in the mean is $1/14$ of $\sigma^2(\bar{f}, t)$.

For detector #2, $\sigma(\bar{f}', t) \sim 0.1$ for $\bar{f}' = 350$ kHz and 650 kHz. Thus the “ion” spectrum of detector #3 is more variable than that of detector #2. This enhanced variability is partially due to precursor activity, which we analyze in Sec. VI. The empirical variance is much larger than the theoretical estimate based on Gaussian statistics because it includes the ELM to ELM variation due to random effects including precursor times. These effects are random in the sense that they vary randomly from ELM to ELM. In previous works, we have included the effect of tokamak to tokamak variation on energy confinement²⁸ and the effect of discharge to discharge variation on the temperature profile shape²⁹.

VI. Time-frequency identification of ELM Precursors

In examining the autoregressive residual fit errors, we identified a number of very

short nonstationary bursts in the one and a half millisecond interval prior to each ELM. The typical duration of the precursor burst is roughly 10 μ sec long. The frequency resolution is only 75 kHz due to short length ($N = 100$) of the segment. Due to its short life, the concept of a spectrum for the precursor is somewhat tenuous.

Figure 12 plots the spectrum of one of the longest (11 μ sec) and most prominent precursors from detector # 3. The precursor is centered at 500 kHz, and occurs 0.45 msec before the second ELM. The dashed line in Fig. 12 is the corresponding estimate on a data segment taken 40 μ sec after the precursor corresponding to the ambient spectrum. In Figure 12, we have used three tapers with a frequency half bandwidth of 75 kHz and then kernel smoothed over an additional 50 kHz half-width.

In comparing the two spectra, we see that the spectrum in the 400-600 kHz range is not only much larger than its normal size, but also larger than the fluctuations in the 1450-1750 kHz range, and this is not typical. The ambient fluctuations in the 1450-1750 kHz range correspond to electron drift direction while the precursor frequency of 500 kHz corresponds to ion drift.

To better quantify the occurrence rate, the duration and strength of the precursor, we have computed the time-frequency distribution for the 4 milliseconds prior to each ELM. To have a very short time resolution, we use only two tapers and smooth over 100 kHz. We compute the mean, $\bar{S}(f)$, and standard deviation, $\sigma(f)$, of the time-frequency distribution averaged over time for each frequency. We standardize the time-frequency plot by subtracting off the mean and dividing by the standard deviation, so that the resulting function is

$$\frac{S_z(f, t) - \bar{S}_z(f)}{\sigma(f)}.$$

We identified two types of short bursts: bursts which are centered in the 250-650 kHz range, and bursts which have a substantial part of their energy content in the 1 MHz range. After inspecting the fourteen time-frequency plots, we concluded that the bursts centered at 1 MHz did not have any noticeable correlation with the onset of the ELMs while the low frequency bursts occur almost exclusively in the one and a half milliseconds prior to the ELM. Furthermore, the bursts in the 1 MHz range occur at a lower amplitude ($10\sigma(f)$) than those in the 250-650 kHz range ($30\sigma(f)$).

To enhance the low frequency fluctuations and to filter out the ambient spectrum centered at 1 MHz, we prewhiten the time series by applying a tenth order autoregressive filter prior to computing the time-frequency distribution. Prewhitening reduces the amplitude of the bursts in the 1 MHz range. For graphical effect, we have set all values of the standardized time-frequency distribution which are less than three to exactly zero.

Figure 13 displays a three-dimensional plot of the prewhitened transformed time-frequency distribution for the four milliseconds immediately prior to the second ELM. The precursor burst at $t = 12.734$ msec is clearly visible and is centered at 500 kHz. Figure 14 presents a similar time-frequency plot for the 4 millisecond time interval just prior to first ELM. The large amplitude, 10 μ sec precursors burst are visible at $t = 5.186$ and 5.56 msec. Only the first burst is visible on the AR residual plot of Fig. 3b. The precursors bursts in the first two ELMs are localized around 500 kHz. However, the frequency range of the precursors for later ELMs varies between 250 kHz and 650 kHz.

Figure 15a plots the integrated energy in the frequency band, [300 – 700] kHz, versus time. The precursor bursts at $t = 5.186$ and 5.56 msec and at $t = 12.734$ msec are clearly visible and above the noise. The ELM oscillations begin at $t = 6.07$ and 13.19 msec. Figure 15b gives the corresponding time history in the [900 – 1100] kHz band. Many fluctuations occur in this frequency band, and there appears to be no correspondence between these fluctuations and the imminent onset of ELM activity. Figure 15c gives the time history in the [1300 – 1700] kHz band, corresponding to electron drift direction. No evidence of precursor activity is indicated. The spectral intensity in this frequency range is virtually constant between ELMs. Thus, Fig. 15 shows that the precursor bursts are localized in the 300 – 700 kHz band.

We set a threshold of $28\sigma(f)$ on the standardized prewhitened time-frequency estimates. We then record all of the events which exceed this magnitude during the four milliseconds immediately prior to each ELM. The threshold value of $28\sigma(f)$ was chosen to give the best identification rate for the ELMs. We find that the amplitudes of the instantaneous bursts have an approximately two-humped distribution, i.e. very few bursts occur with amplitudes of 18–30 $\sigma(f)$. Thus, we can change the threshold from $15\sigma(f)$ to $30\sigma(f)$ and only slightly reduce the success rate of predicting ELMs.

Table 3 summarizes our findings on the ELM precursor bursts. Column 2 gives the time until the next ELM. Column 3 gives the maximum burst amplitude in $\sigma(f)$ and Column 4 gives the characteristic frequency of the burst. Column 5 gives the duration in μ sec. The seventh ELM has a number of bursts in the 250-650 kHz, but they have relatively small amplitude and therefore do not exceed the threshold. The eleventh ELM has a high amplitude burst at 1350 kHz instead of in the 300-600 kHz range. The large amplitude, low frequency burst after the 10th ELM is not listed in Table 3 because it occurs more than 4 milliseconds before the next ELM.

The shorter duration (2-11 μ sec) of these precursors is probably due to a combination of physics differences, the fast sampling rate on the TFTR diagnostic, and our high resolution estimation procedure. *The short duration of the precursor events re-*

duces their physical significance as a cause of the ELMs and probably means that they are more of a symptom of a change in plasma conditions as the stability boundary is approached. We also caution that our analysis only applies to this particular TFTR discharge and that other discharges may be different.

These short precursor bursts occur only in detector #3, and we have found no corresponding phenomena in detector #2. One explanation is that the precursors are occurring at the plasma edge and that the scattering volume for detector #2 is too far in the plasma interior to sense the precursors. Alternatively, the absence of precursors in detector #2 could be due to the difference in measured k values of the two detectors.

We have examined several other discharges, and the phenomena of high frequency bursts in the ion drift direction appears to be robust. In several of the other discharges, the precursors were weaker and less reliable.

VII. Summary

In this article, we described several techniques which we have found useful in examining the nonstationary bursts: autoregressive filters to isolate nonstationary phenomena, prewhitening to reduce bias, and the singular value decomposition to isolate the fundamental components of the signal, including the spectrum during the ELMs. We have used a high resolution smoothed multitaper estimate of the evolutionary spectrum to isolate short-lived high frequency ELM precursor bursts. Our evolutionary spectra estimate uses many fewer degrees of freedom than in our previous work for two reasons: first, the bursts are so transient that segment lengths of more than 100 points blur the time resolution; second, the events appear to be coherent (i.e. consist only of a single mode), and thus are easier to estimate than an ensemble of transient modes.

Our main experimental findings are: 1) the ELM spectrum is more symmetric and broader than the stationary spectrum; 2) the existence of high frequency ELM “ion” precursor bursts; 3) the “electron” spectrum returns to its ambient value within a half a millisecond after the ELM while the “ion” spectrum grow by a factor of eight between ELMs; 4) the onset of the ELMs appears correlated with the level of ion fluctuations (for detector #3); 5) growth rates of $0.1\text{--}0.5\text{ msec}^{-1}$ are estimated after the end of an ELM. Results 3-5 are not always present in other discharges. In some discharges, the “electron” spectrum grows between ELMs and the “ion” spectrum is saturated.

Figure 9 shows that the “ion” spectrum grows exponentially between ELMs. When the ion fluctuation spectrum increases more slowly, the onset of the ELM is delayed. It appears that when the “ion” spectrum reaches a critical level, the ELM is triggered. However, this “critical level” varies by 40 %. The onset of the ELM need not be caused by the increased fluctuation level. Instead, both phenomena may be caused by the same destabilizing mechanism. Some other discharges have a fixed level for the ion spectrum, and have no indication of an ion character to the ELM onset.

The electron drift spectrum also appears to grow exponentially to a critical level and then enters a slow growth phase. The initial “electron” growth rates are faster in detector #3 than in detector #2, but the length of time of rapid growth is longer in detector #2; thus the total increase in the electron spectrum is the nearly the same in both detectors. *Because the spectrum grows exponentially between ELMs, we interpret this as the linear phase of the plasma instabilities and the 0.1-0.5 msec⁻¹ growth rates to be the linear instability growth rates.* Our interpretation is based on the assumption that nonlinear saturation is an algebraic function of time. Similarly, if the turbulence level were evolving slowly due to changing plasma conditions, such as changes in the electric field²⁰⁻²¹, the spectrum would almost certainly be evolving more slowly than exponentially.

The precursor bursts, which we identify, have much shorter lifetime than previously reported measurements^{2,4}, and are intermittent. Their high frequency, ion drift nature further suggests that the ELM onset is related to increased ion turbulence. Intermittent fluctuation bursts occur at other frequencies, especially near 1 MHz. However, these bursts occur at a lower level ($10\sigma(f)$ instead of $30\sigma(f)$), and are not correlated with the onset of an ELM burst. We note that the precursors on this TFTR discharge occur with sufficient regularity that the occurrence of the next ELM can be predicted with about 80% accuracy. For this to be of use in fusion reactor design, we must hope that the same precursor signature occurs in other devices and in most discharges.

Acknowledgements

We thank R. Nazikian for many interesting discussions which stimulated this work and for providing the data used in this analysis. We thank the TFTR group for allowing us to analyze the microwave scattering data. The work of KSR and AS was funded by the U.S. Department of Energy, Grant No. DE-FG02-86ER53223.

Bibliography

1. ASDEX team, *Nuclear Fusion* **39**, 1959 (1989).
2. C. Bush, N. Bretz, R. Nazikian, B.C. Stratton, E. Synakowski, G. Taylor, R. Budny, A.T. Ramsey, S.D. Scott, M. Bell, R. Bell, H. Biglari, M. Bitter, D.S. Darrow, P. Efthimion, R. Fonck, E.D. Fredrickson, K. Hill, H. Hsuan, S. Kilpatrick, K.M. McGuire, D. Manos, D. Mansfield, S.S. Medley, D. Mueller, Y. Nagayama, H. Park, S. Paul, S. Sabbagh, J. Schivell, M. Thompson, H.H. Towner, R.M. Wieland, M.C. Zarnstorff, and S. Zweben, "Characteristics of the TFTR limiter H-mode: the transition, ELMs, transport and confinement," Submitted for publication in *Nuclear Fusion*.
3. S.M. Kaye, J. Manickam, N. Askura, R.E. Bell, Yun-Tung Lau, B. LeBlanc, C.E. Kessel, H.W. Kugel, S.F. Paul, S. Sesnic, H. Takahashi, *Nuclear Fusion* **30**, 2621 (1990).
4. K. McGuire, V. Arunasalam, C.W. Barnes, M.G. Bell, M. Bitter, R. Boivin, N.L. Bretz, R. Budny, C.E. Bush, A. Cavallo, T.K. Chu, S.A. Cohen, P. Colestock, S.L. Davis, D.L. Dimock, H.F. Dylla, P.C. Efthimion, A.B. Ehrhardt, R.J. Fonck, E. Fredrickson, H.P. Furth, G. Gammel, R.J. Goldston, G. Greene, B. Grek, L.R. Grisham, G. Hammett, R.J. Hawryluk, H.W. Hendel, K.W. Hill, E. Hinnov, D.J. Hoffman, J. Hosea, R.B. Howell, H. Hsuan, R.A. Hulse, A.C. Janos, D. Jassby, F. Jobs, D.W. Johnson, L.C. Johnson, R. Kaita, C. Kieras-Phillips, S.J. Kilpatrick, P.H. LaMarche, B. LeBlanc, D.M. Manos, D.K. Mansfield, E. Mazzucato, M.P. McCarthy, M.G. McCune, D.H. McNeill, D.M. Meade, S.S. Medley, D.R. Mikkelsen, D. Monticello, R. Motley, D. Mueller, J.A. Murphy, Y. Nagayama, R. Nazikian, E.B. Neischmidt, D.K. Owens, H. Park, W. Park, S. Pitcher, A.T. Ramsey, M.H. Redi, A.L. Roquemore, P.H. Rutherford, G. Schilling, J. Schivell, G.L. Schmidt, S.D. Scott, J.C. Sinnis, J. Stevens, B.C. Stratton, W. Stodiek, E.J. Synakowski, W.M. Tang, G. Taylor, J.R. Timberlake, H.H. Towner, M. Ulrickson, S. von Goeler, R. Wieland, M. Williams, J.R. Wilson, K.-L. Wong, M. Yamada, S. Yoshikawa, K.M. Young, M.C. Zarnstorff, and S.J. Zweben, *Phys. Fluids B* **2**, 1287 (1990).
5. E.J. Doyle, R.J. Groebner, K.H. Burrell, P. Gohil, T. Lehecka, N.C. Luhmann, Jr., H. Matsumoto, T.H. Osborne, W.A. Peebles, and R. Philipona, *Phys. Fluids B* **3**, 2300 (1991).

6. H. Zohm, F. Wagner, M. Endler, J. Gernhardt, E. Holzhauser, W. Kerner, V. Mertens, *Nuclear Fusion* **32**, 489 (1992).
7. C. Bush, J. Schivell, G. Taylor, N. Bretz, A. Cavallo, E. Fredrickson, A. Janos, D. Mansfield, K. McGuire, R. Nazikian, H. Park, A.T. Ramsey, B.C. Stratton, and E. Synakowski, *Rev. Sci. Instr.* **61**, 35 (1990).
8. D.J.Grove and D.M. Meade, *Nuclear Fusion* **25**, 1167 (1985).
9. K.S. Riedel, A. Sidorenko, D.J. Thomson, "Spectral estimation of plasma fluctuations I: Comparison of methods," Published in this issue, *Physics of Plasmas* **1** page ? (1994).
10. N. Bretz, P. Efthimion, J. Doane, and A. Kritz, *Rev. Sci. Instr.* **59**, 1538 (1988).
11. N. Bretz, R. Nazikian, W. Bergin, M. McCarthy, *Rev. Sci. Instr.* **61**, 3031 (1990).
12. N. Bretz, R. Nazikian, and K. Wong, *Proceedings of the 17th European Phys. Soc. Conf.*, (European Phys. Soc., Amsterdam, 1990) p. 1544.
13. P.J. Brockwell and R.A. Davis, *Time series - theory and methods*. (Springer Verlag, New York 1991).
14. M.B. Priestley, *Spectral analysis and time series*. (Academic Press, New York 1981).
15. M.B. Priestley, *J. Roy. Stat. Soc. Ser. B* **27**, 204 (1965).
16. K.S. Riedel, *I.E.E.E. Trans. on Signal Processing* **41**, 2439 (1993).
17. D.J. Thomson, *Proc. I.E.E.E.* **70**, 1055 (1982).
18. J. Park, C.R. Lindberg, and F.L. Vernon, *J. Geophys. Res.* **92B**, 12,675 (1987).
19. D.J. Thomson and A.D. Chave, in *Advances in spectrum analysis*, edited by S. Haykin, (Prentice-Hall, New York 1990) Ch. 2, pg. 58-113.
20. R.J. Groebner, K.H. Burrell, and R.P. Seraydarian, *Phys. Rev. Lett.* **64**, 3015 (1990).

21. R.J. Groebner, W.A. Peebles, K.H. Burrell, T.N. Carlstrom, P. Gohil, R.P. Seraydarian, E.J. Doyle, R. Philipona, H. Matsumoto, B. Cluggish, *Proceedings of the Thirteenth Conference on Plasma Physics and Controlled Fusion Research*, IAEA-CN-531A-VI-4 (International Atomic Energy Agency, Vienna 1991) p. 453.
22. B. Kleiner, R.D. Martin and D.J. Thomson, *J. Royal Stat. Soc. Series B*, **41**, 313 (1979).
23. R.D. Martin and D.J. Thomson, *Proc. I.E.E.E.*, **70**, 1096 (1982).
24. D.J. Thomson, *Phil. Trans. R. Soc. Lond. A*, **330**, 601(1990).
25. C. Nardone, *Plasma Physics and Controlled Fusion*, **34**, 1447 (1992)
26. H. Zohm, J.M. Greene, L.L. Lao, & E.J.Strait, "Mirnov coil analysis in the D-IIID tokamak using the singular value decomposition method." G.A. Report GA-A20886, Submitted to Nuclear Fusion, (1992).
27. K.S. Riedel, E. Eberhagen, O. Gruber, K. Lackner, G. Becker, O. Gehre, V. Mertens, J. Neuhauser, F. Wagner, and the ASDEX team, *Nuclear Fusion* **28**, p. 1509 (1988).
28. K.S. Riedel, *Nuclear Fusion* **30**, 755, (1990).
29. P.J. McCarthy, K.S. Riedel, O.J.W.F. Kardaun, H. Murmann, K. Lackner, *Nuclear Fusion* **31**, 1595, (1991)

Table 1: ELM and quiescent period duration

ELM #	Quiescent time (msec)	Duration of ELM (msec)	Total period (msec)
1	4.45	1.92	6.37
2	5.2	0.8	6
3	4.08	1.4	5.48
4	5.38	0.8	6.18
5	7.71	1.0	8.71
6	4.46	1.55	6.01
7	7.21	1.1	8.31
8	5.73	1.39	7.12
9	6.6	2.12	8.72
10	6.3	1.26	7.56
11	9.44	1.11	10.55
12	5.64	0.6	6.24
13	7.19	1.14	8.33
14	5.75	0.85	6.6
Mean	6.08 (5.82)	1.22	7.3 (7.05)
Std. dev.	1.46 (1.14)	0.43	1.45 (1.15)

The mean and standard deviation in parentheses are computed by excluding the interval between the tenth and eleventh ELMs.

Table 2: Critical ion log-spectrum levels

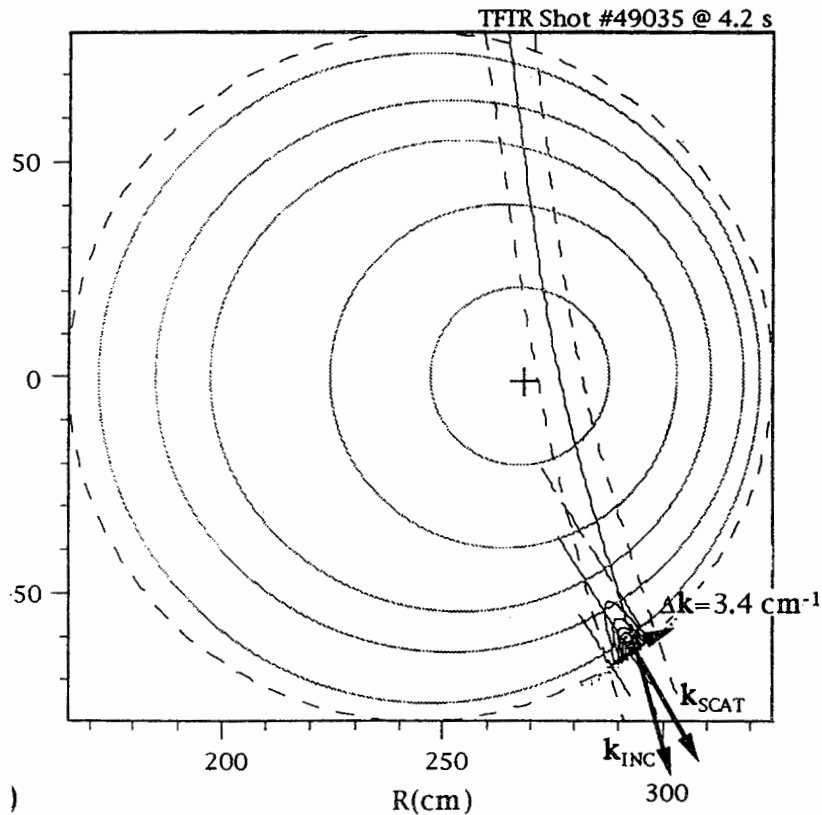
ELM #	200–500 kHz	500–800 kHz
1	2.19	3.54
2	2.51	3.54
3	2.50	3.68
4	2.59	3.41
5	2.37	3.32
6	2.42	3.54
7	2.30	3.30
8	2.23	3.27
9	2.16	3.22
10	2.41	3.44
11	2.50	3.47
12	2.51	3.44
13	2.55	3.72
14	2.39	3.40
Mean	2.40	3.45
Std. dev.	0.14	0.15

The critical level of the ion fluctuations is calculated by averaging $\log_{10}[\hat{S}(\bar{f}, t)]$ over 0.44 msec.

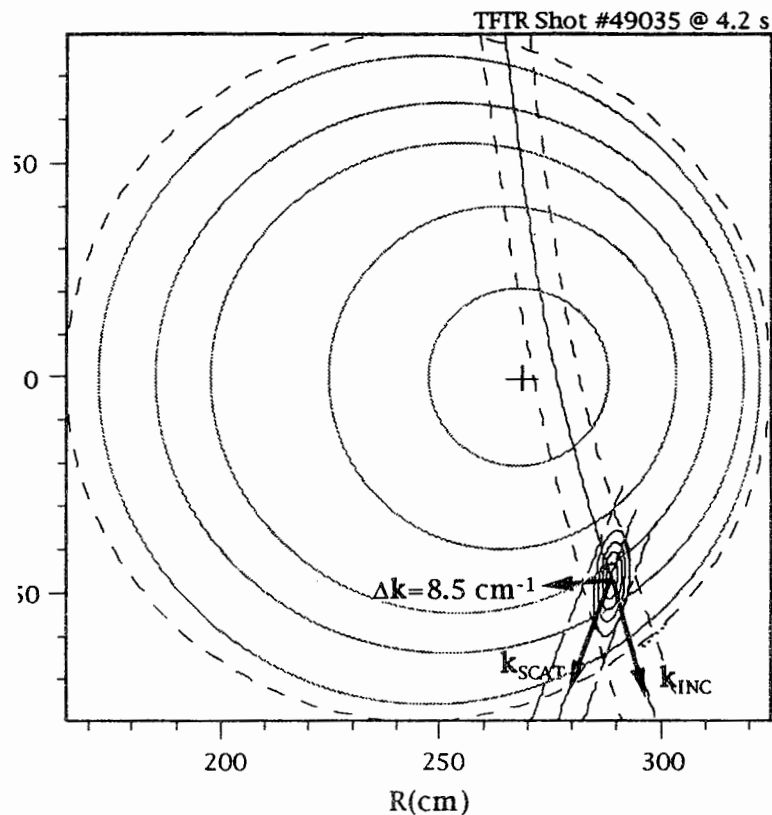
Table 3: Ion precursor bursts

ELM #	Time until ELM (millisec)	Amplitude ($\sigma(f)$)	Frequency (kHz)	Duration (μ sec)
1	0.88	35	300–800	2
1	0.51	31	650	2
2	0.45	35	500	11
3	1.14	65	300	6
3	0.80	50	400	4
3	0.56	89	600	7
4	0.37	34	400	2
5	1.04	90	200–700	6
6	0.24	36	650	8
8	1.49	42	450	10
9	1.12	52	350	3
10	1.44	19	500	3
11	0.49	29	1350	2
12*	.1-.2	27	200- 550	-
13	1.83	37	500	6
13	0.54	37	750	3
14	0.13	43	200–600	3

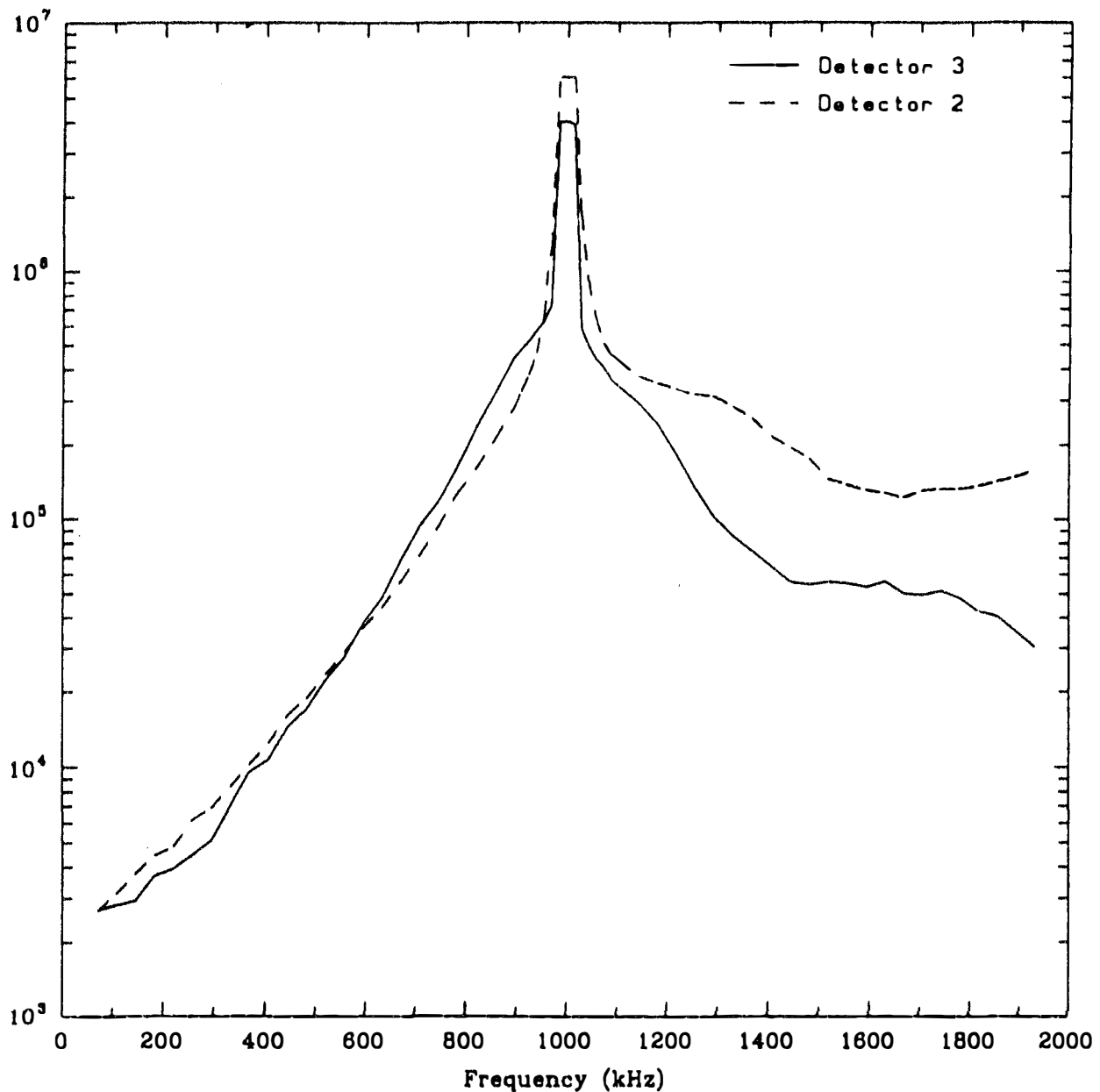
* No identifiable mode, only broad-banded activity above threshold



)



(a) Ray tracing calculation of the extraordinary mode wave path launched from the top of the vacuum vessel. The center of the beam path is the central curve while the outer curves mark the beam half-width of Detector #3 is at the bottom of the vacuum vessel, and the line of sight of the detector is displayed as well. Detector #3 measures $|k_{\text{inc}}| \simeq 3.3 \text{ cm}^{-1}$ and k is parallel to the poloidal magnetic field at 0 ± 0.1 . (b) Line of sight for detector #2 and ray tracing calculation of the extraordinary mode. Detector #2 measures fluctua-



2. Smoothed spectrum of entire 524 288 point segment, estimated 20 orthogonal tapers with $w = 0.1$ kHz and then kernel smoothed 20 kHz. The central peak at 1 MHz is partially coherent and correlates to the receiver intermediate frequency caused by wall and wave-e reflections. The local broadening from 1450 to 1750 kHz is due to na fluctuations which are rotating in the electron drift wave direc-We normalize the spectrum of detector #2 such that the two spectra the same amplitude when the broadening of the 1 MHz line begins. "ion" spectra are identical while the "electron" spectrum of detector is three times larger.

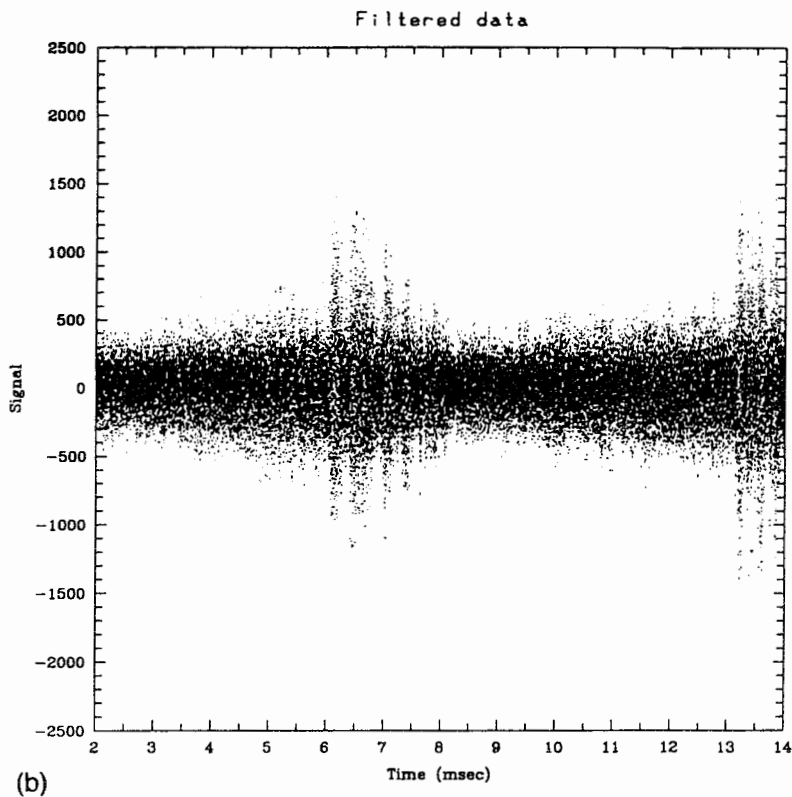
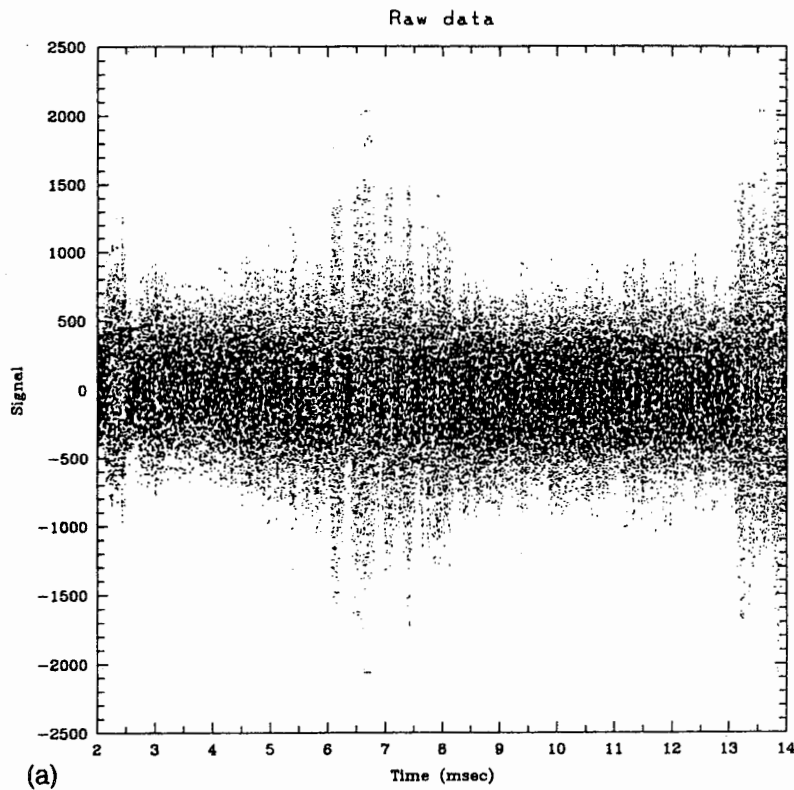
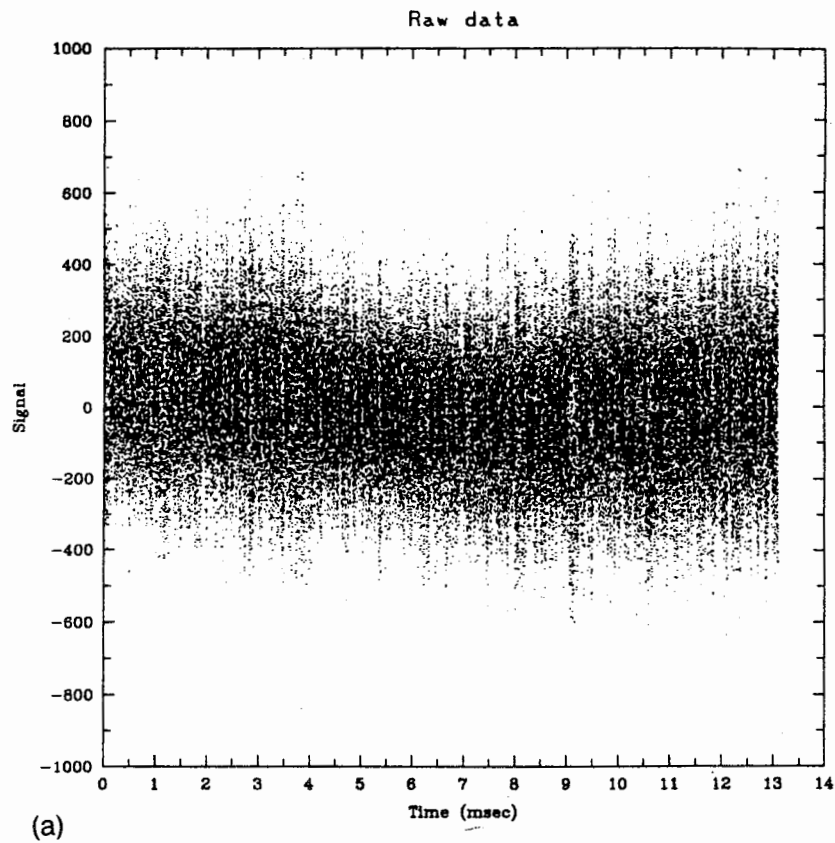
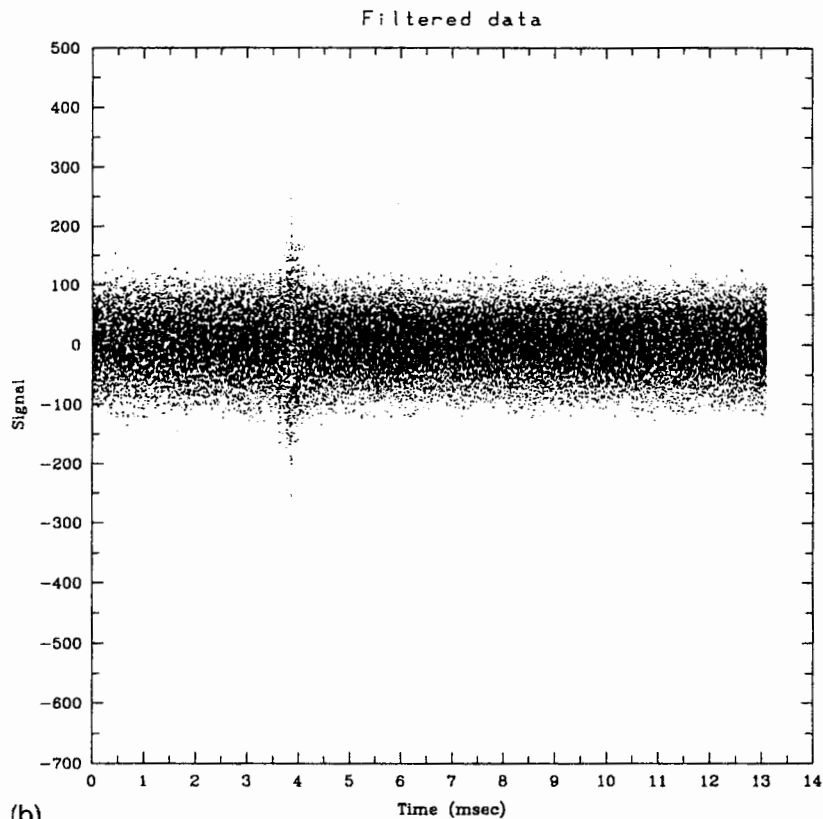


FIG. 3. (a) The 12 ms data segment from $t=2$ ms to $t=14$ ms of the microwave scattering diagnostic for TFTR discharge #49035. The ELM's occur at $t=6.07$ and 13.19 ms. A number of fluctuation bursts prior to the ELM are visible; however, most of these bursts are due to changes in the 1 MHz frequency range. Two precursor bursts in the 250–650 kHz range occur at $t=5.186$ and 12.734 ms; however, it is difficult to distinguish these bursts from the IF frequency bursts. (b) Filtered data after using a tenth-order autoregressive filter. Since the saw-tooth spectrum is broader than the ambient spectrum, the ELM amplitude is enhanced relative to the background level. The intermittent bursts which are concentrated in the 1 MHz range are reduced by filtering. In contrast, the two precursor bursts in the 300–600 kHz range, at $t=5.186$ and 12.734 ms, have been enhanced.



(a)



(b)

Fig. 4. (a) Microwave scattering data for TFTR discharge #50616. A sawtooth occurs at $t=3.86$ ms and is barely visible. The variance appears to be growing linearly in time. (b) Filtered data after using a tenth order Butterworth progressive filter. Since the sawtooth spectrum is broader than the dominant spectrum, the effect of the sawtooth is greatly enhanced by filtering. The linear growth of the variance is eliminated by filtering. This indicates that the nonstationarity is concentrated in the 1 MHz peak.

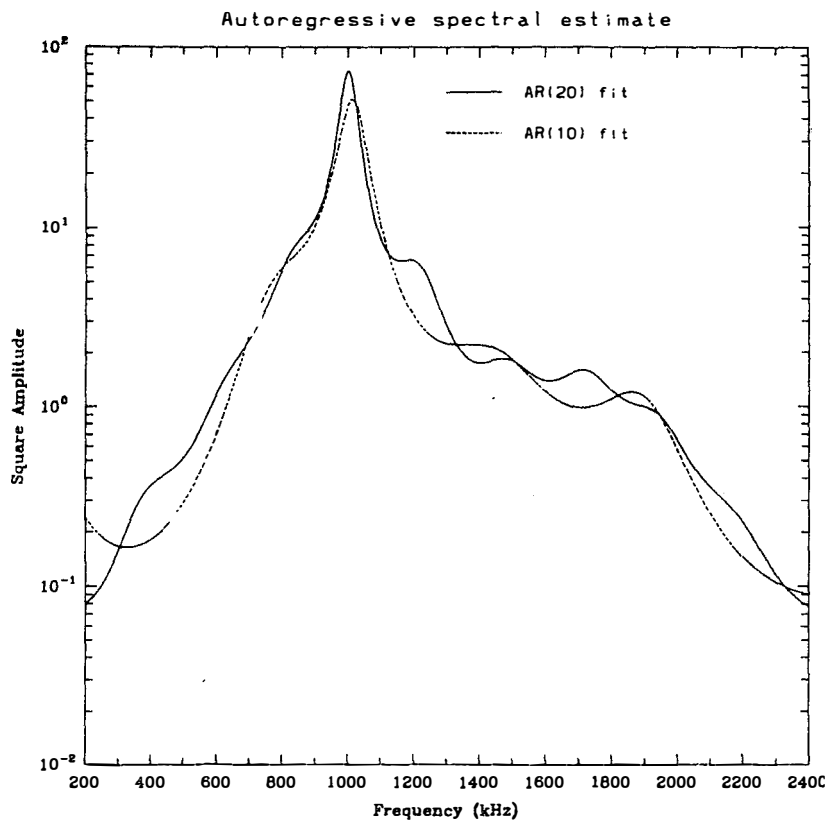


FIG. 5. Autoregressive estimate spectrum of entire data set, estimated by the method of moments. The 1 MHz peak is artificially broadened due to model misfit.

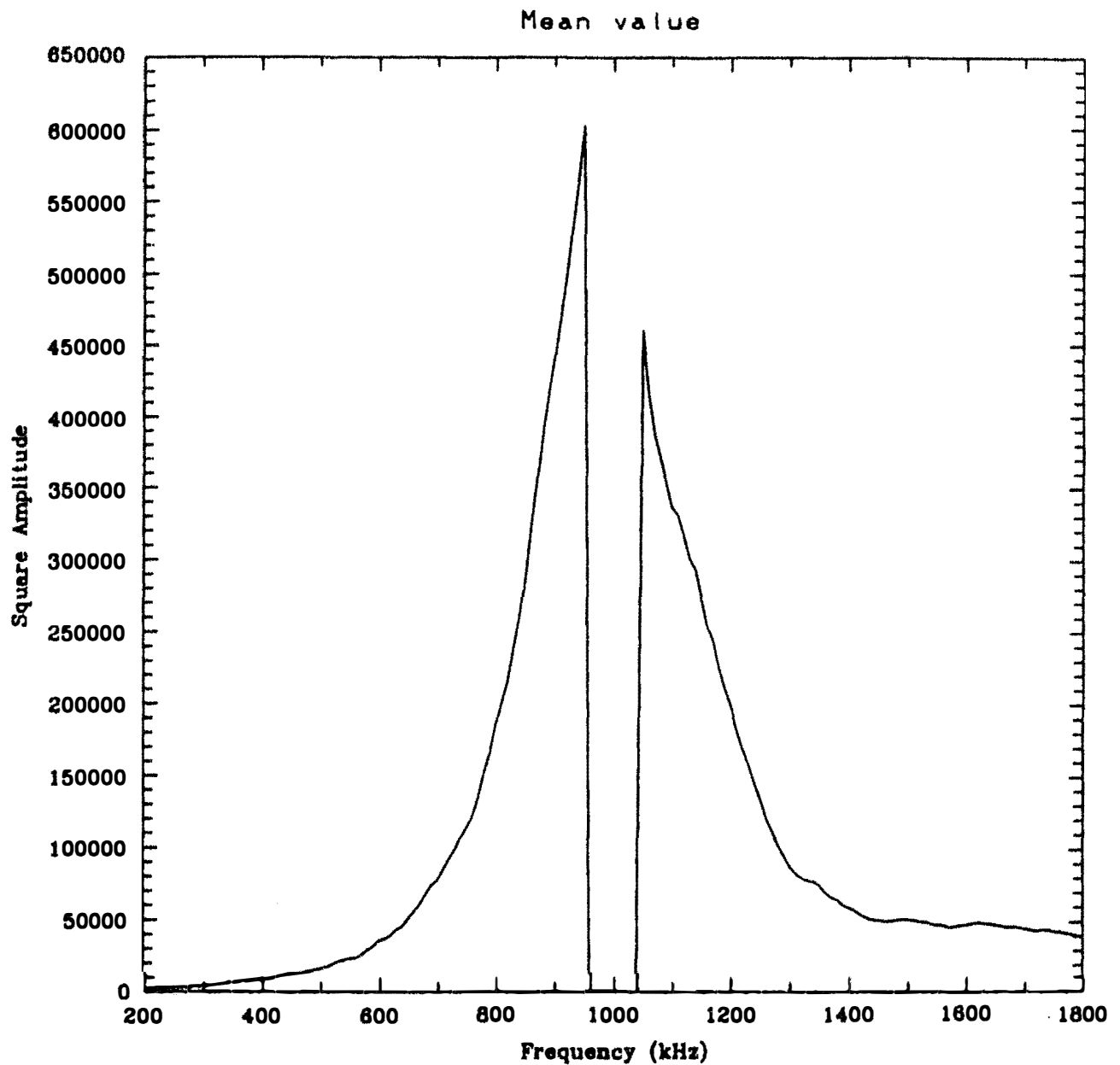


FIG. 6. Mean spectral estimate, $\bar{S}(f)$ of the time-frequency distribution, $S(f,t)$, estimated using 1000 point samples with eight tapers ($w=20$ kHz) and then kernel smoothed over 20 kHz. The mean spectrum is broader than the estimated spectrum in Fig. 2 because the frequency resolution is lower.

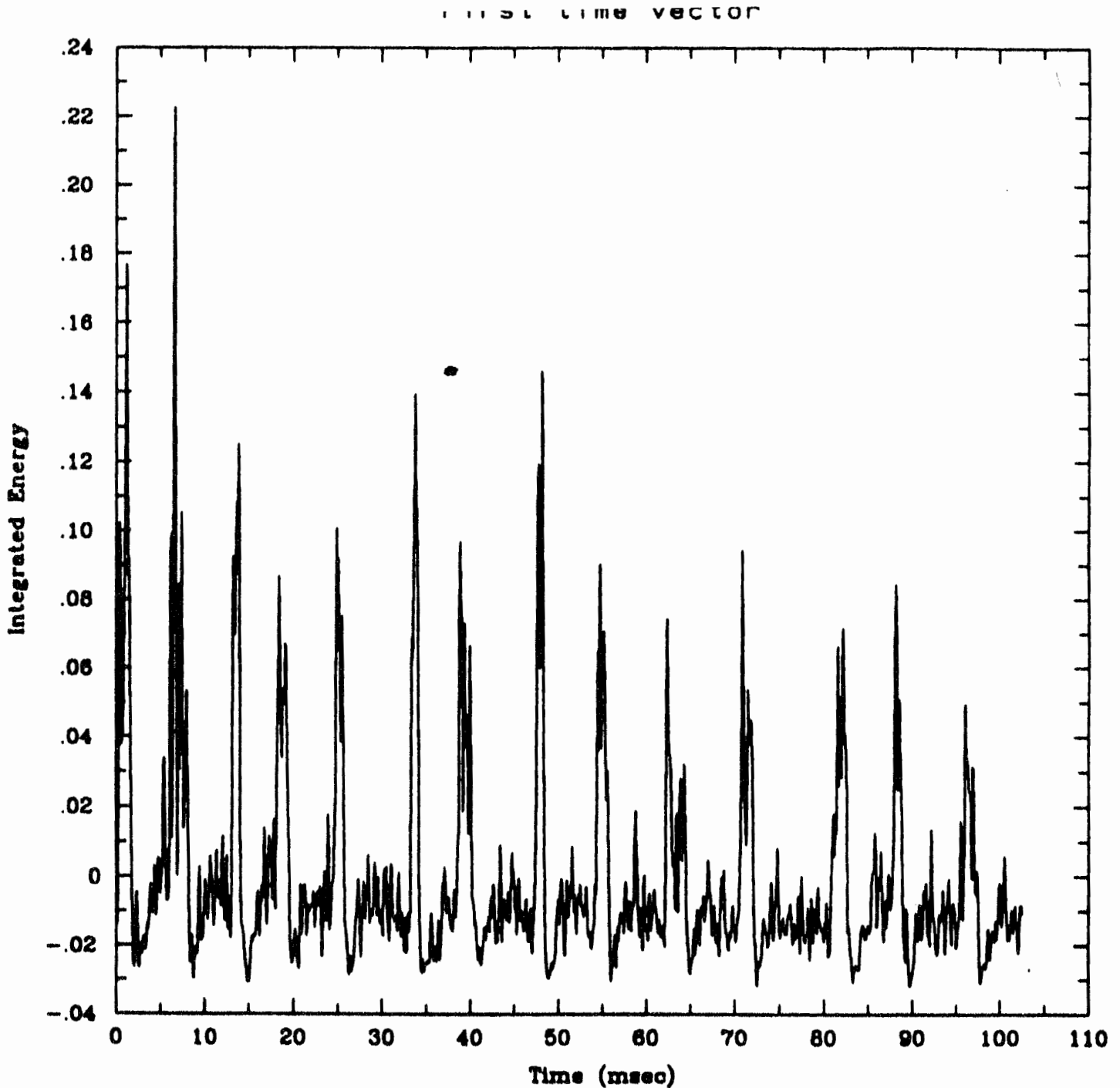
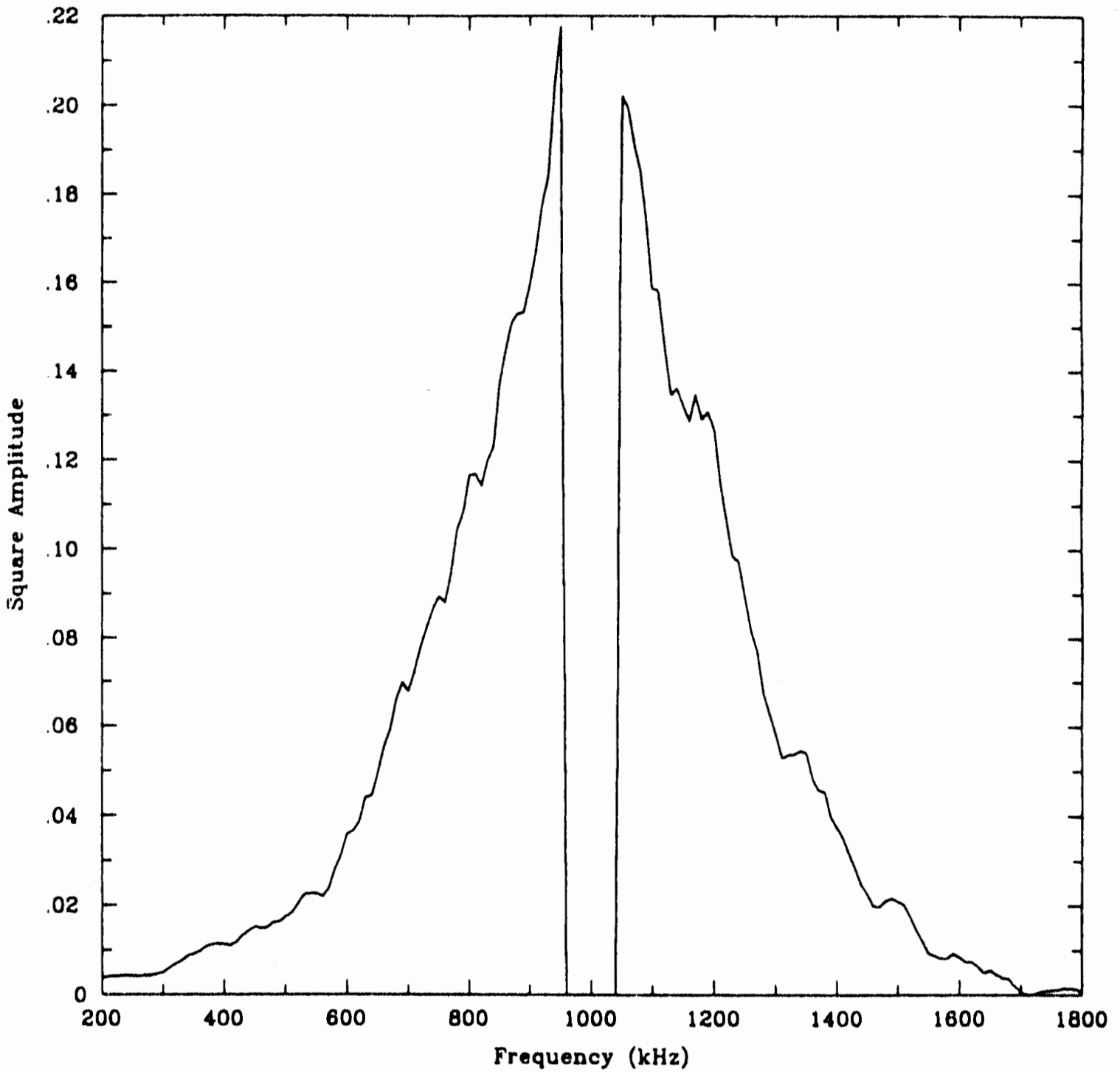


FIG. 7. First time vector of the singular value decomposition of the time-frequency distribution. Each of the 14 peaks corresponds to an ELM burst. The rise time of the ELM's in Fig. 7 is significantly longer than the actual rise time because we have reduced the time resolution to increase the frequency resolution in Fig. 8. We remove the IF frequency at 1 MHz prior to computing the singular value decomposition.

first frequency vector



G. 8. First frequency vector of the singular value decomposition of the α_e -frequency distribution. The spectrum during the ELM is broader and more symmetric than the mean spectrum of Fig. 6.

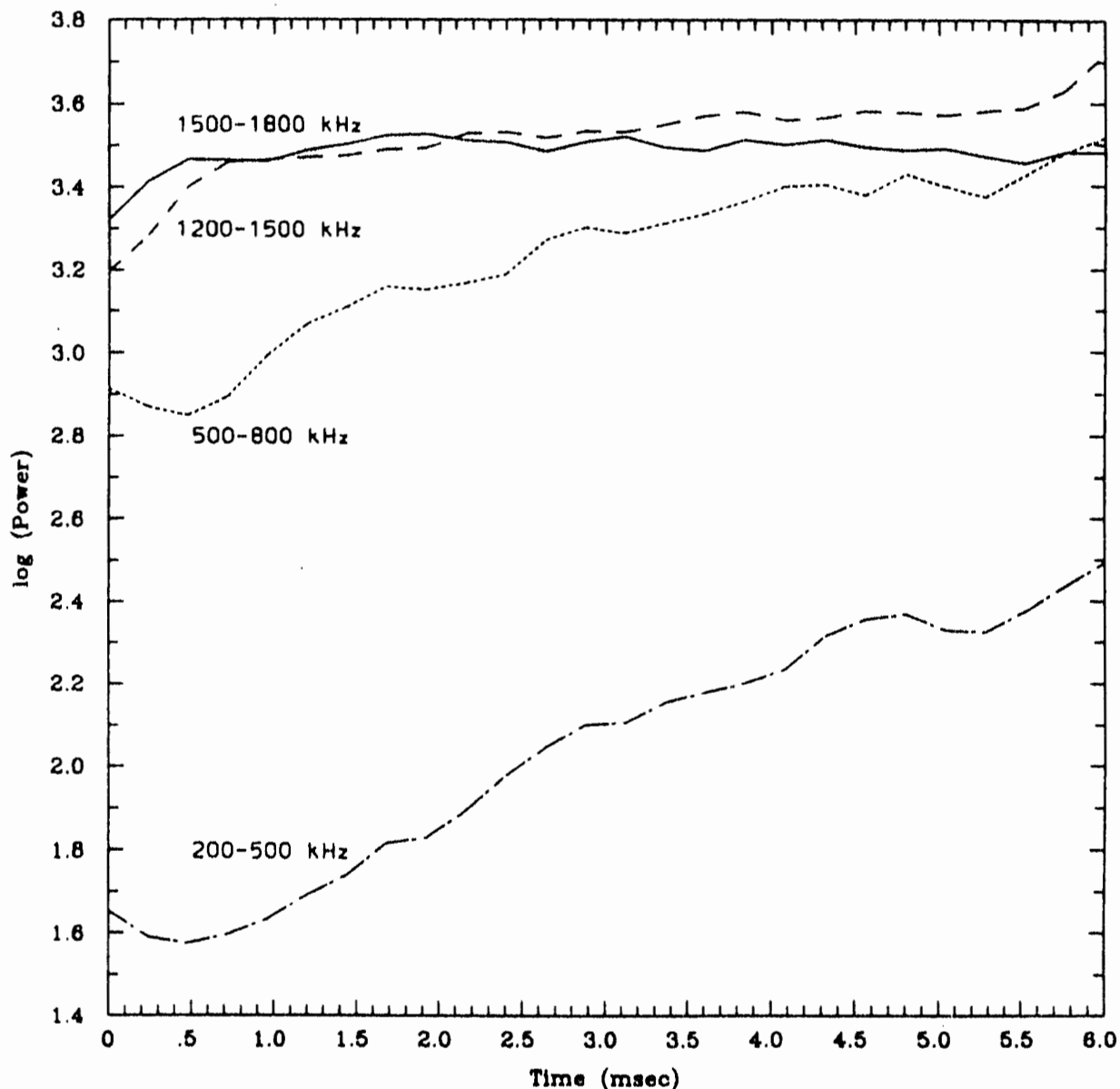


FIG. 9. $\hat{S}(\bar{f}, t) \equiv \int_{\bar{f}-150 \text{ kHz}}^{\bar{f}+150 \text{ kHz}} \mathcal{S}(f, t) df$ of detector #3, averaged over the 14 quiescent periods. The quiescent periods are standardized to a length of 5.8 ms. Since the curves are nearly straight, the growth rates of the ion fluctuations are exponential. When the lengths of the 13 intervals are not standardized to be the same length, more complicated dependencies result. The fluctuations in the electron drift direction increase rapidly in the first 0.5 ms after the ELM subsides. During the next 5.3 ms, the level of the electron drift fluctuations is virtually constant. In contrast, the fluctuation level in the ion drift direction increases by a factor of 5 in the 500–800 kHz range and by a factor of 8 in the 200–500 kHz range. During this time, the growth rates are $\gamma = 0.2 \text{ ms}^{-1}$ for f in 200–500 kHz, and $\gamma = 0.15 \text{ ms}^{-1}$ for f in 500–800 kHz. When the “ion” spectrum grows more slowly, the onset of the ELM is delayed.

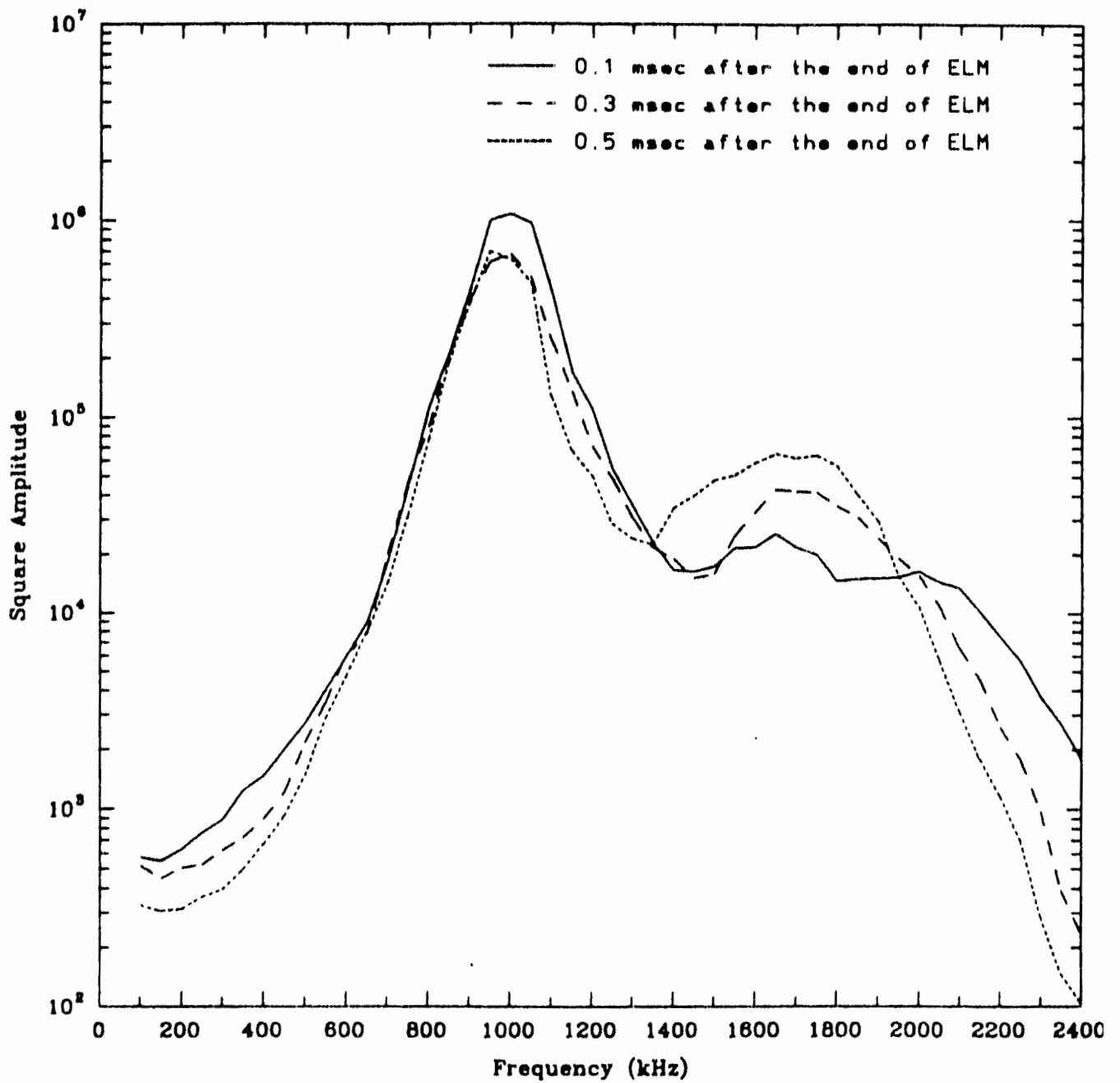


FIG. 10. Spectrum for three time slices 0.1, 0.3, and 0.5 ms after second ELM. The “electron” spectrum between 1600 and 1800 kHz growing noticeably. The 1 MHz peak decreases in amplitude and width. This narrowing of the 1 MHz line results in a reduction of “ion” spectrum. In detector #2, the corresponding secondary maximum does not grow appreciably after the end of the ELM. The spectra were calculated with 8 tapers on 1000 data point segments, and have a frequency resolution of 20 kHz and a time resolution of 0.1 ms.

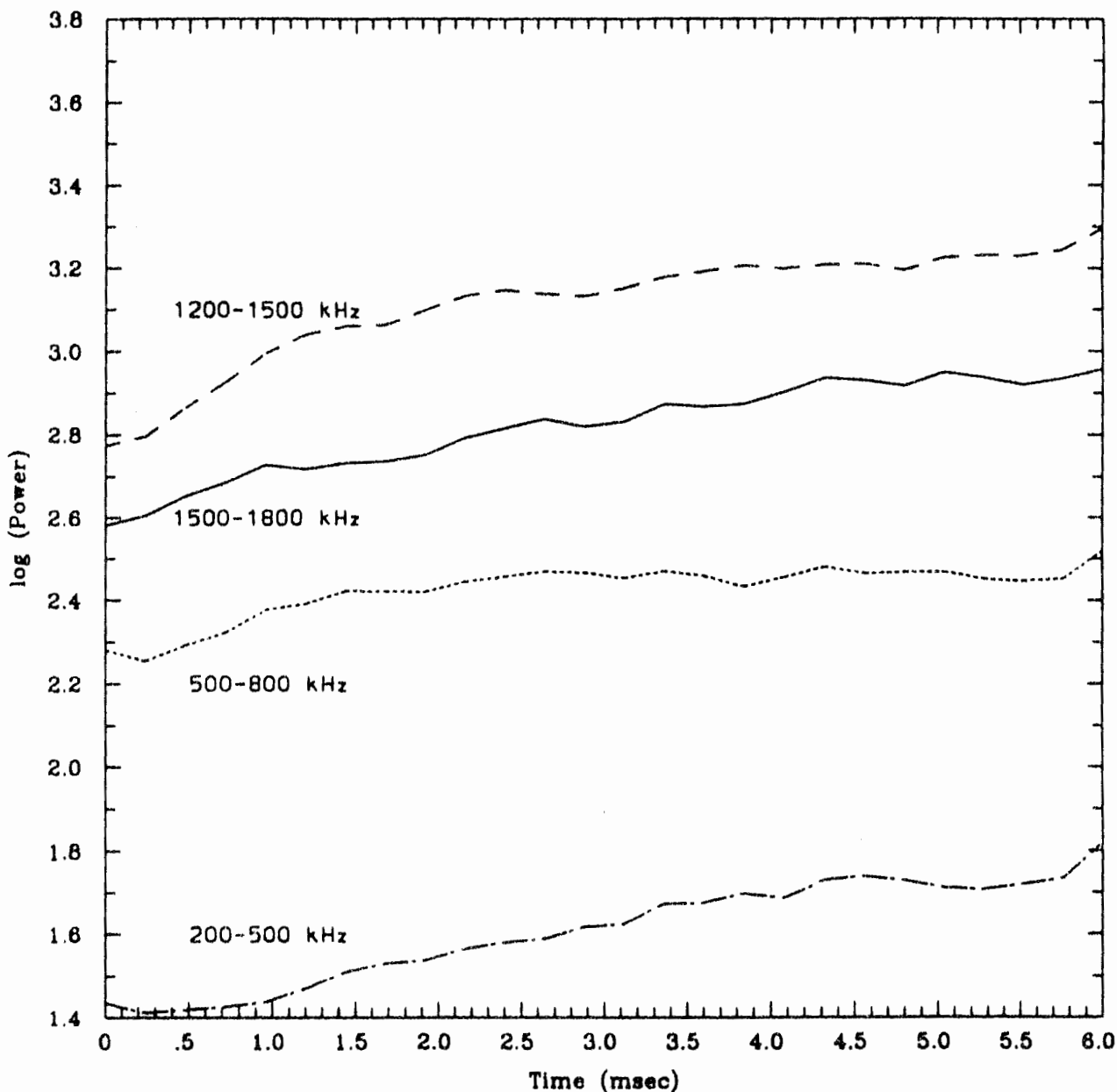


FIG. 11. $\bar{S}(\bar{f}, t) \equiv \int_{\bar{f}-150 \text{ kHz}}^{\bar{f}+150 \text{ kHz}} S(f, t) df$ of detector #2, averaged over the 14 quiescent periods. In the first millisecond, the “electron” spectrum grows by 50% for f' in 1500–1800 kHz and by 100% for f' in 1200–1500 kHz. (We continue to use $f' \equiv 1\text{MHz} - f$ for detector #2.) For detector #2, $\gamma = 0.28 \text{ ms}^{-1}$ for f in 1200–1500 kHz, and $\gamma = 0.24 \text{ ms}^{-1}$ for f in 1500–1800 kHz. After this initial phase, the “electron” growth rates slow by a factor of 3–5. The “ion” spectrum increases by $1.6 \times$ in the 500–800 kHz range and by $2.2 \times$ in the 200–500 kHz range. In detector #2, the “electron” spectrum is larger than in detector #3 and the growth of the ion spectral energy between ELM is less: $\gamma = 0.1 \text{ ms}^{-1}$ for f' in 200–500 kHz; for f' in 500–800 kHz, $\gamma = 0.17 \text{ ms}^{-1}$ for the time 0.3 to 1.3 ms after the ELM and $\gamma = 0.01 \text{ ms}^{-1}$ for later times. Thus the “ion” spectrum

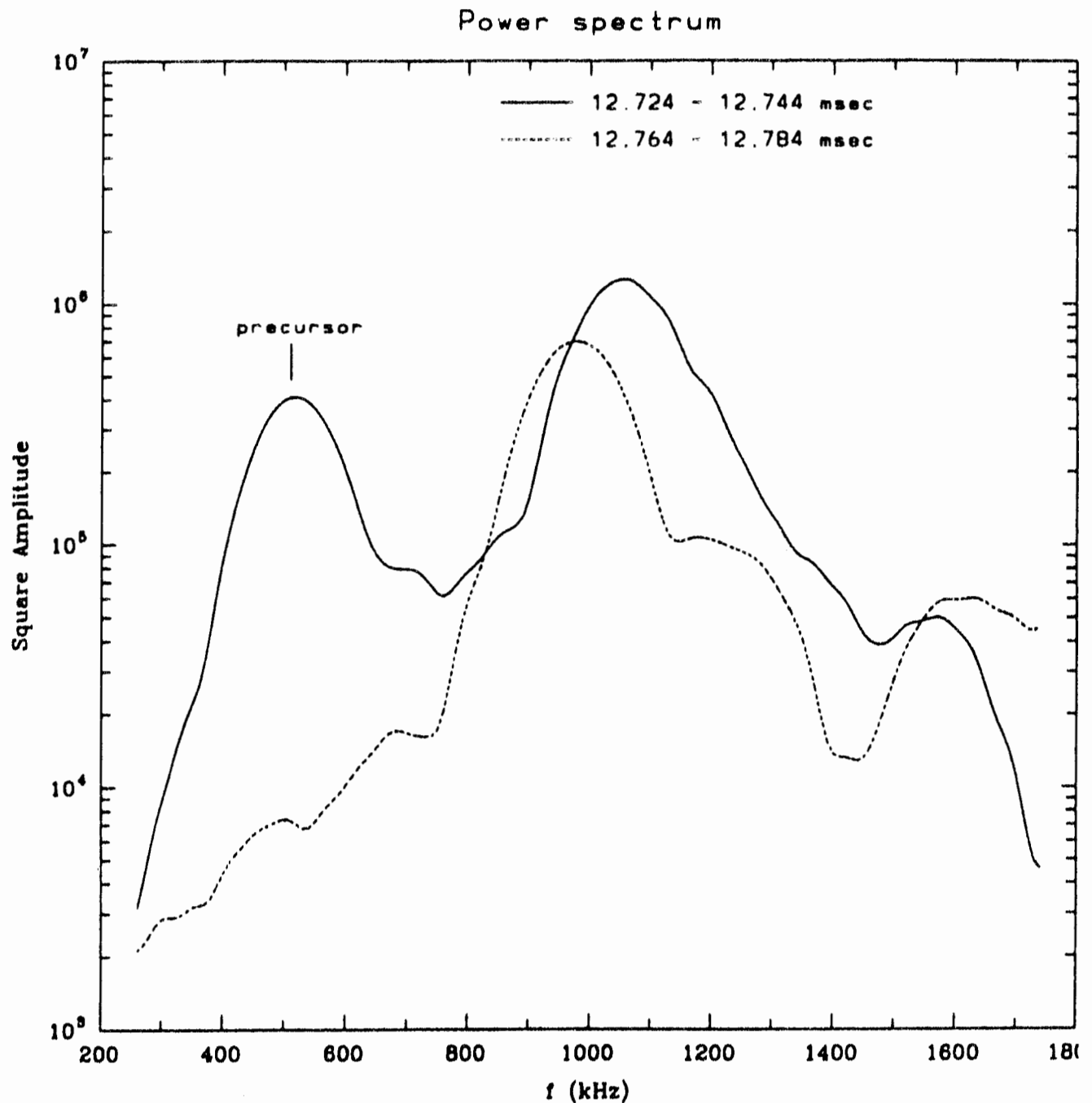


FIG. 12. Estimated spectral density during a precursor 0.45 ms before second ELM. The secondary peak at 500 kHz occurs only during precursors. This precursor is particularly long lived and resolvable. Spectrum is computed on a 100-point segment using 3 tapers with a bandwidth of 75 kHz followed by a kernel smoother with a half-width of 50 kHz. Dashed line: Corresponding estimated spectral density for the 100-point segment 40 μ s later. The precursor peak has totally disappeared and spectrum has returned to its ambient shape. Since the frequency resolution of Fig. 12 is less than that of Fig. 5, the spectrum in Fig. 12 correspondingly broader (just as the spectrum in Fig. 6 is broader than

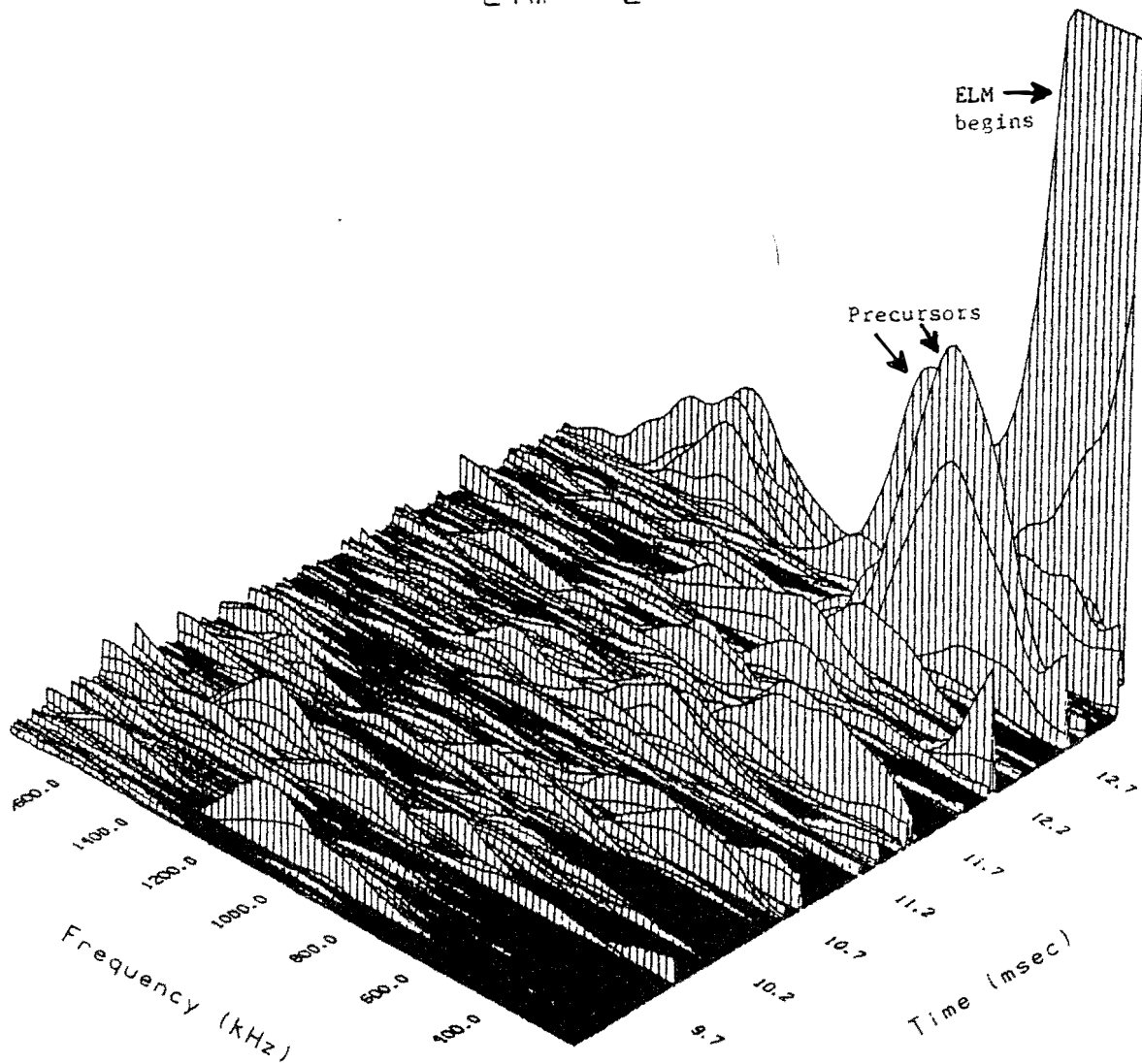


FIG. 13. Time-frequency distribution of the 4 ms time interval prior to the second ELM. The large amplitude, $10 \mu\text{s}$ precursors burst is visible at $t = 12.734 \text{ ms}$. The data has been filtered using a tenth order autoregressive filter to reduce the spectral range. Prewhitening removes the fluctuations which are associated with nonstationary activity of the central 1 kHz peak. The evolutionary spectrum is computed on 50-point segments with 50% overlap. We use two Slepian tapers with a bandwidth of 100 kHz followed by a kernel smoother with a kernel half-width of 100 kHz.

Elm # 1

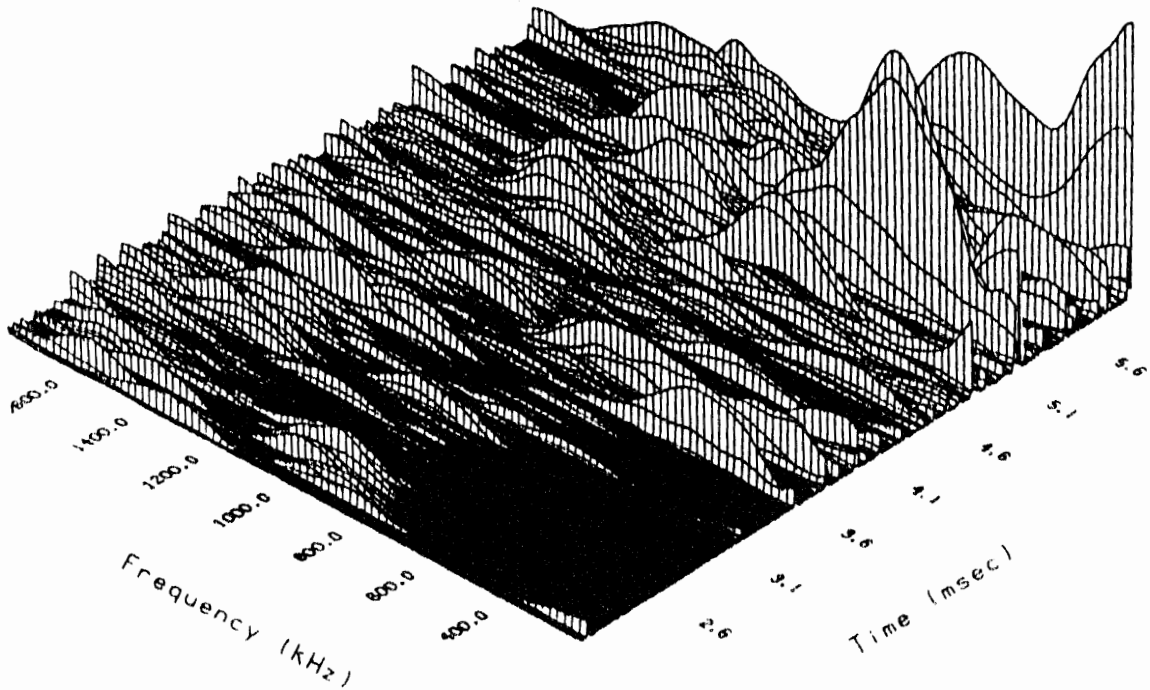
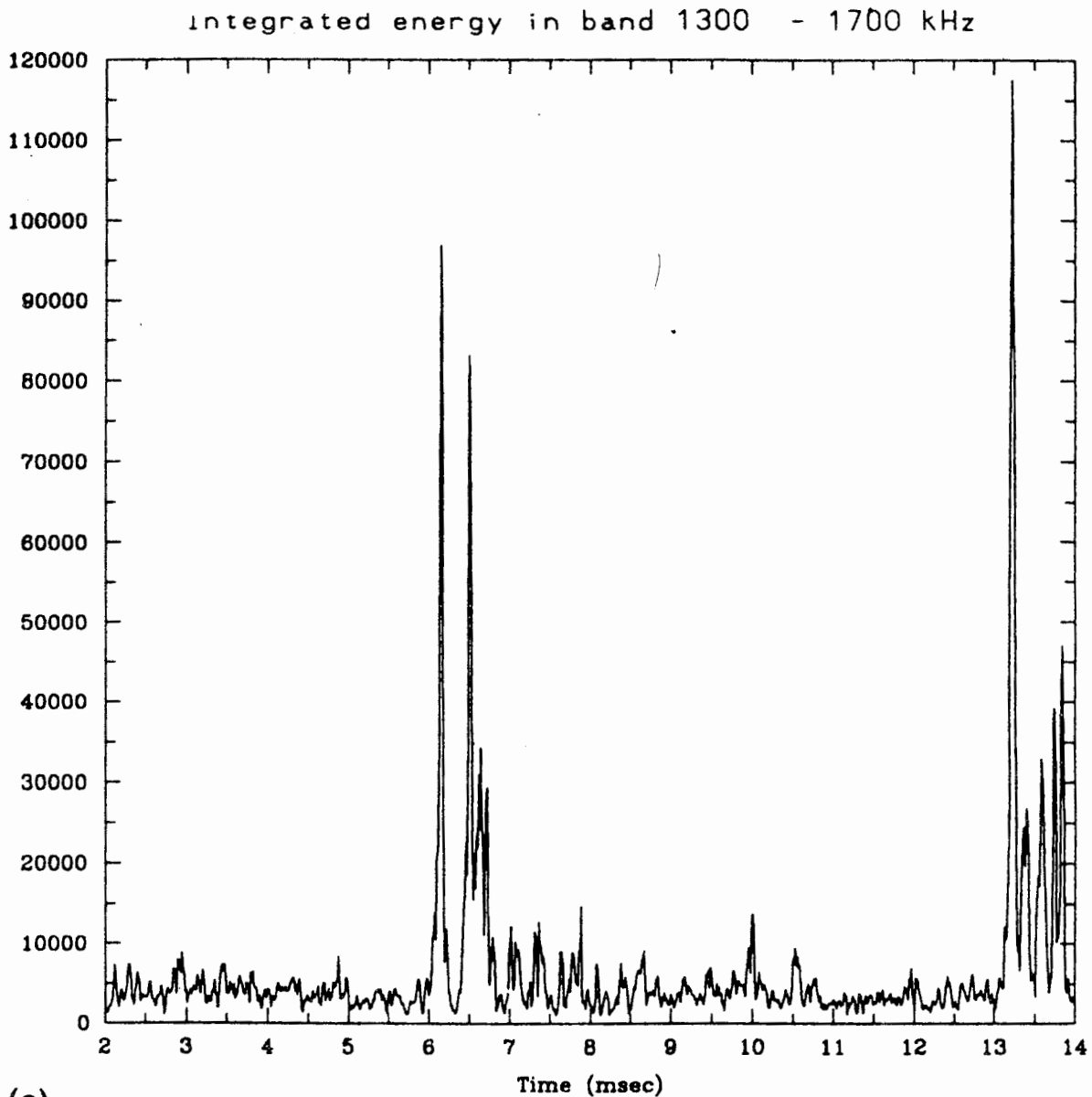
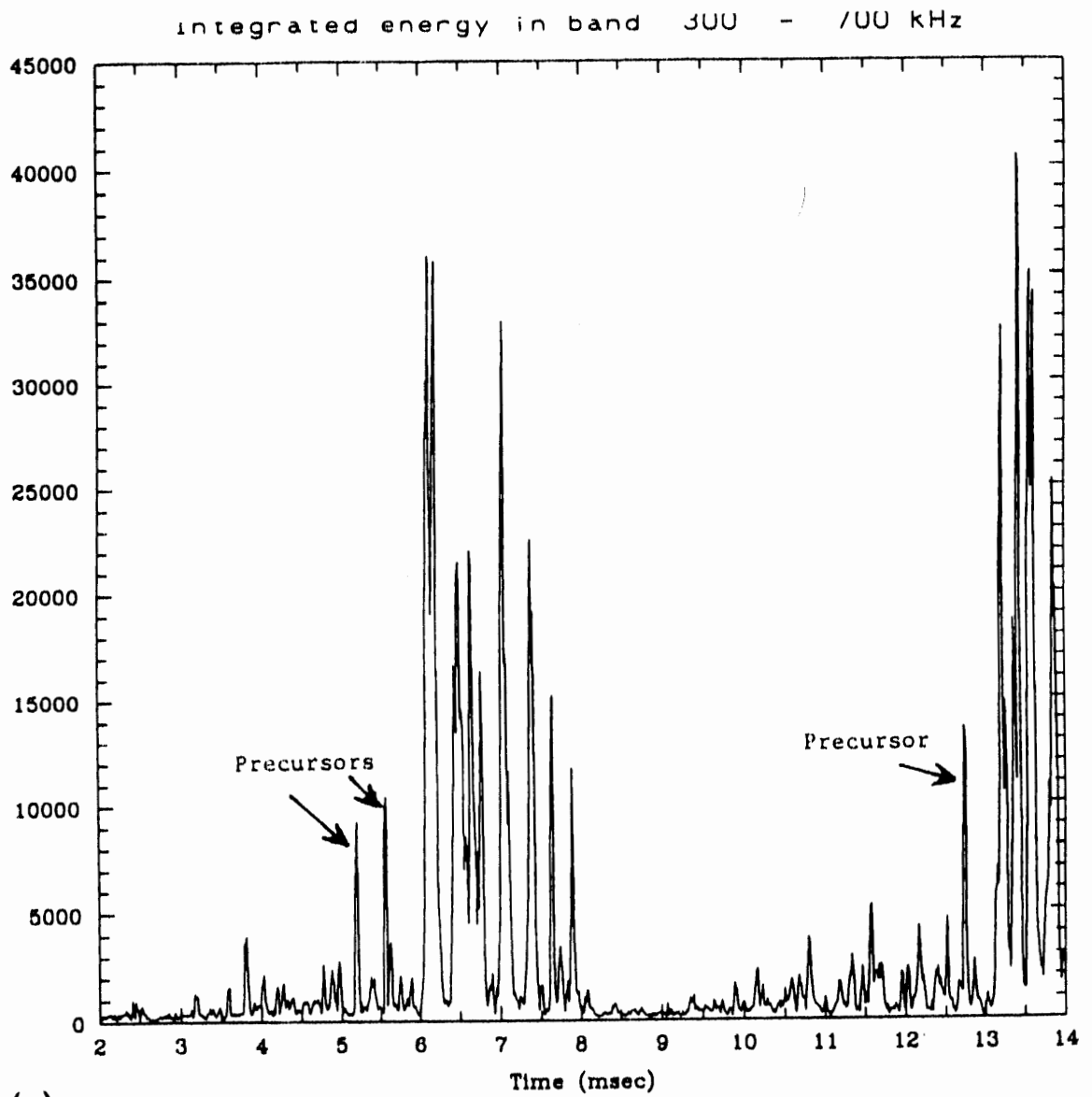


FIG. 14. Time-frequency distribution of the prewhitened data for the 4 ms time interval just prior to first ELM. The large amplitude, $10 \mu\text{s}$ precursors bursts are visible at $t = 5.186$ and 5.56 ms. Only the first burst is visible on the ΔR residual plot of Fig. 3(b).

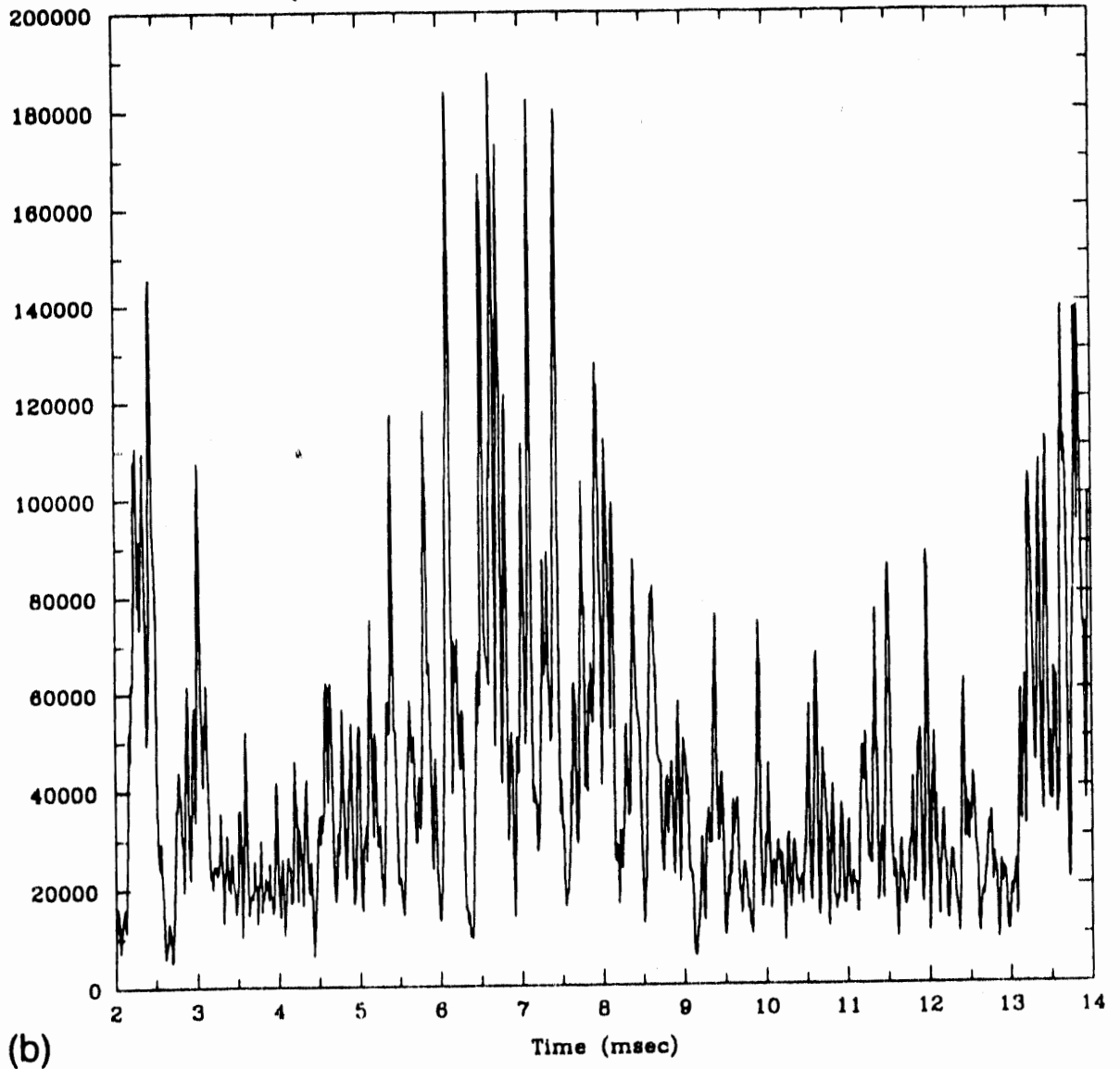


(c)

Fig. 15. Integrated energy in the frequency band [300–700] kHz versus time for the first two ELM's. The precursor bursts are clearly visible in the 300–700 kHz band. (b) Integrated energy in two frequency bands [0–1100] kHz versus time. The numerous bursts in the IF frequency band occur with no clear pattern, and thus are ill-suited to forecast ELM activity. (c) Integrated energy in the frequency band [1300–1700] kHz versus time. The precursor bursts are barely visible in the electron drift frequency band.



(a)



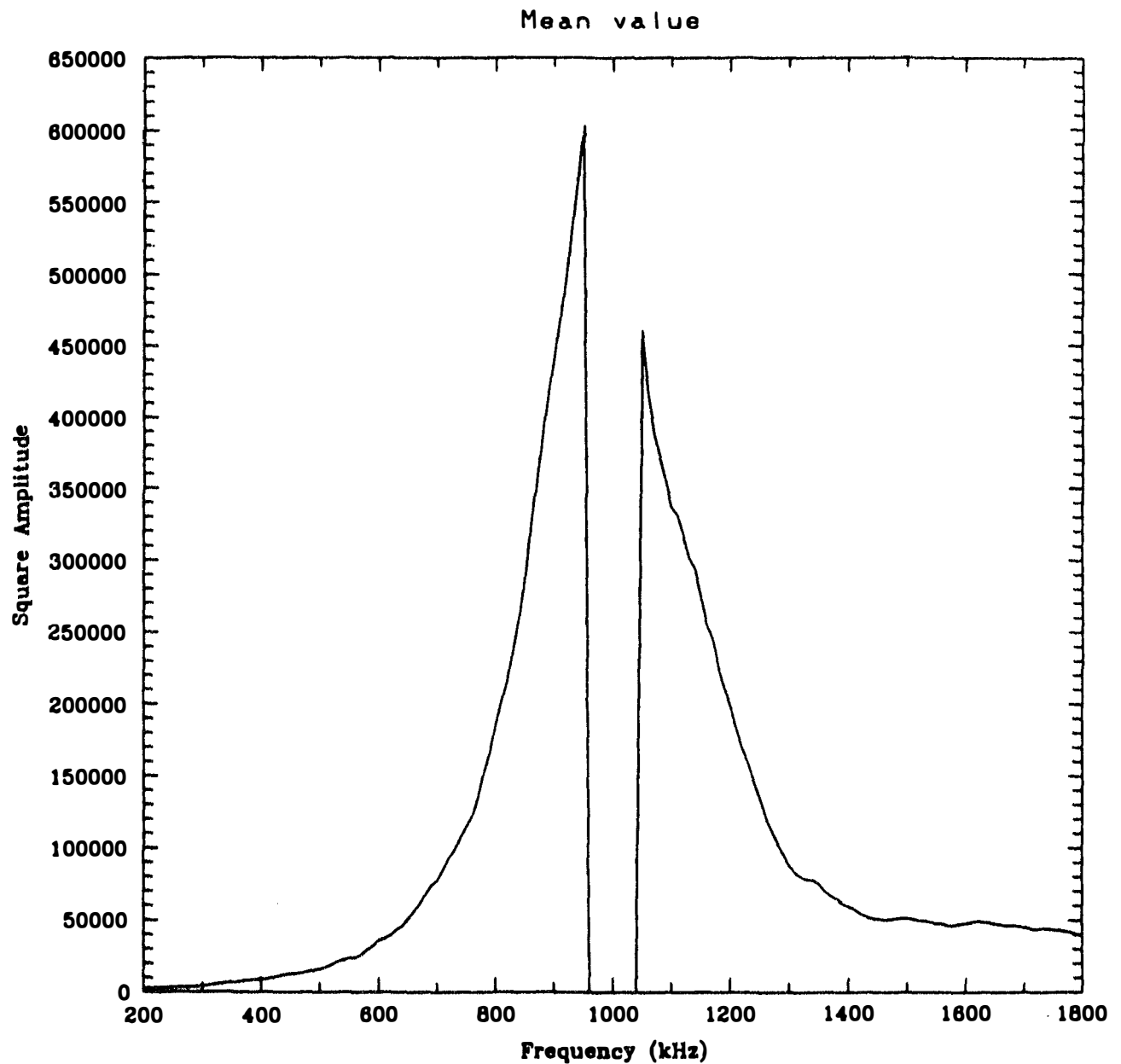


FIG. 6. Mean spectral estimate, $\bar{S}(f)$ of the time-frequency distribution, $S(f,t)$, estimated using 1000 point samples with eight tapers ($w=20$ kHz) and then kernel smoothed over 20 kHz. The mean spectrum is broader than the estimated spectrum in Fig. 2 because the frequency resolution is lower.

Figure Captions:

Figure 1a: Ray tracing calculation of the extraordinary mode wave path launched from the top of the vacuum vessel. The center of the beam path is the central curve while the outer curves mark the beam half-width of 5.0 cm. Detector #3 is at the bottom of the vacuum vessel, and the line of sight of the detector is displayed as well. Detector #3 measures $|\vec{k}_{scat} - \vec{k}_{inc}| \simeq 3.3 \text{ cm}^{-1}$ and \vec{k} is parallel to the poloidal magnetic field at $\frac{r}{a} \simeq 1.0 \pm 0.1$.

Figure 1b: Line of sight for detector #2 and ray tracing calculation of launched extraordinary mode. Detector #2 measures fluctuations somewhat farther in the plasma interior, at $\frac{r}{a} \simeq 0.75 \pm 0.1$ with $|\vec{k}_{scat} - \vec{k}_{inc}| \simeq 8.5 \text{ cm}^{-1}$.

Figure 2: Smoothed spectrum of entire 524,288 point segment, estimated with 20 orthogonal tapers with $w = 0.1 \text{ kHz}$ and then kernel smoothed over 20 kHz. The central peak at 1 MHz is partially coherent and corresponds to the receiver intermediate frequency caused by wall and waveguide reflections. The local broadening from 1450 kHz to 1750 kHz is due to plasma fluctuations which are rotating in the electron drift wave direction. We normalize the spectrum of detector #2 such that the two spectra have the same amplitude when the broadening of the 1 MHz line begins. The “ion” spectra are identical while the “electron” spectrum of detector #2 is three times larger.

Figure 3a: The 12 millisecond data segment from $t = 2 \text{ msec}$ to $t = 14 \text{ msec}$ of the microwave scattering diagnostic for T.F.T.R. discharge # 49035. The ELMs occur at $t = 6.07$ and 13.19 msec . A number of fluctuation bursts prior to the ELM are visible; however, most of these bursts are due to changes in the 1 MHz frequency range. Two precursor bursts in the 250 – 650 kHz range occur at $t = 5.186$ and 12.734 msec ; however, it is difficult to distinguish these bursts from the IF frequency bursts.

Figure 3b: Filtered data after using a tenth order autoregressive filter. Since the sawtooth spectrum is broader than the ambient spectrum, the ELM amplitude is enhanced relative to the background level. The intermittent bursts which are concentrated in the 1 MHz range are reduced by filtering. In contrast, the two precursor bursts in the 300 – 600 kHz range, at $t = 5.186$ and 12.734 msec , have been enhanced.

Figure 4a: Microwave scattering data for TFTR discharge # 50616. Sawtooth

occurs at $t = 3.86$ msec and is barely visible. The variance appears to be growing linearly in time.

Figure 4b: Filtered data after using a tenth order autoregressive filter. Since the sawtooth spectrum is broader than the ambient spectrum, the effect of the sawtooth is greatly enhanced by filtering. The linear growth of the variance is eliminated by filtering. This indicates that the nonstationarity is concentrated in the 1 MHz peak.

Figure 5: Autoregressive estimate spectrum of entire data set, estimated by the method of moments. The 1 MHz peak is artificially broadened due to model misfit.

Fig. 6: Mean spectral estimate, $\bar{S}(f)$ of the time-frequency distribution, $S(f, t)$, estimated using 1000 point samples with eight tapers ($w = 20$ kHz) and then kernel smoothed over 20 kHz. The mean spectrum is broader than the estimated spectrum in Fig. 2 because the frequency resolution is lower.

Fig. 7: First time vector of the singular value decomposition of the time-frequency distribution. Each of the 14 peaks corresponds to an ELM burst. The rise time of the ELMs in Fig. 7 is significantly longer than the actual rise time because we have reduced the time resolution to increase the frequency resolution in Fig. 8. We remove the IF frequency at 1 MHz prior to computing the singular value decomposition.

Fig. 8: First frequency vector of the singular value decomposition of the time-frequency distribution. The spectrum during the ELM is broader and more symmetric than the mean spectrum of Fig. 6.

Fig. 9: $\bar{S}(\bar{f}, t) \equiv \int_{\bar{f}-150kHz}^{\bar{f}+150kHz} S(f, t)df$ of detector # 3, averaged over the 14 quiescent periods. The quiescent periods are standardized to a length of 5.8 msec. Since the curves are nearly straight, the growth rates of the ion fluctuations are exponential. When the lengths of the 13 intervals are not standardized to be the same length, more complicated dependencies result.

The fluctuations in the electron drift direction increase rapidly in the first 0.5 msec after the ELM subsides. During the next 5.3 msec, the level of the electron drift fluctuations is virtually constant. In contrast, the fluctuation level in the ion drift direction increases by a factor of five in the 500-800 kHz range and by a factor of eight in the 200-500 kHz range. During this time, the growth rates are $\gamma = 0.2$ msec⁻¹ for f in 200 – 500 kHz, and $\gamma = 0.15$ msec⁻¹ for f in 500 – 800 kHz. When the “ion” spectrum grows more slowly, the onset of the ELM is delayed.

Fig. 10: Spectrum for three time slices 0.1, 0.3, and 0.5 msec after the second ELM. The “electron” spectrum between 1600 and 1800 kHz is growing noticeably. The 1 MHz peak decreases in amplitude and in width. This narrowing of the 1 MHz line results in a reduction of the “ion” spectrum. In detector #2, the corresponding secondary maximum does not grow appreciably after the end of the ELM. The spectra were calculated with 8 tapers on 1000 data point segments, and have a frequency resolution of 20 kHz and a time resolution of 0.1 msec.

Fig. 11: $\bar{S}(\bar{f}, t) \equiv \int_{\bar{f}-150kHz}^{\bar{f}+150kHz} S(f, t)df$ of detector # 2, averaged over the 14 quiescent periods. In the first millisecond, the “electron” spectrum grows by 50 % for f' in 1500 – 1800 kHz and by 100 % for f' in 1200 – 1500 kHz. (We continue to use $f' \equiv 1\text{MHz} - f$ for detector #2.) For detector #2, $\gamma = 0.28 \text{ msec}^{-1}$ for f in 1200 – 1500 kHz, and $\gamma = 0.24 \text{ msec}^{-1}$ for f in 1500 – 1800 kHz. After this initial phase, the “electron” growth rates slow by a factor of three to five. The “ion” spectrum increases by $1.6 \times$ in the 500-800 kHz range and by $2.2 \times$ in the 200-500 kHz range. In detector #2, the “electron” spectrum is larger than in detector #3 and the growth of the ion spectral energy between ELM is less: $\gamma = 0.1 \text{ msec}^{-1}$ for f' in 200 – 500 kHz; for f' in 500 – 800 kHz, $\gamma = 0.17 \text{ msec}^{-1}$ for the time 0.3 to 1.3 msec after the ELM and $\gamma = 0.01 \text{ msec}^{-1}$ for later times. Thus the “ion” spectrum appears to be more important near the plasma edge.

Fig. 12: Estimated spectral density during a precursor 0.45 msec before the second ELM. The secondary peak at 500 kHz occurs only during the precursors. This precursor is particularly long lived and resolvable. Spectrum is computed on a 100-point segment using 3 tapers with a bandwidth of 75 kHz followed by a kernel smoother with a half-width of 50 kHz.

Dashed line: Corresponding estimated spectral density for the 100-point segment 40 μsec later. The precursor peak has totally disappeared and the spectrum has returned to its ambient shape. Since the frequency resolution of Fig. 12 is less than that of Fig. 5, the spectrum in Fig. 12 is correspondingly broader (just as the spectrum in Fig. 6 is broader than the spectrum in Fig. 2).

Figure 13: Time-frequency distribution of the 4 millisecond interval prior to the second ELM. The large amplitude, 10 μsec precursors burst is visible at $t = 12.734$ msec. The data has been filtered using a tenth order autoregressive filter to reduce the spectral range. Prewhitening removes the fluctuations which are associated with nonstationary activity of the central 1 MHz peak. The evolutionary spectrum is

computed on 50-point segments with 50 % overlap. We use two Slepian tapers with a bandwidth of 100 kHz followed by a kernel smoother with a kernel half-width of 100 kHz .

Figure 14: Time-frequency distribution of the prewhitened data for the 4 mil-lisec time interval just prior to first ELM. The large amplitude, 10 μ sec precursors bursts are visible at $t = 5.186$ and 5.56 msec. Only the first burst is visible on the AR residual plot of Fig. 3b.

Figure 15a: Integrated energy in the frequency band [300 – 700] kHz versus time for the first two ELMs. The precursor bursts are clearly visible in the 300 – 700 kHz band.

Figure 15b: Integrated energy in two frequency band [900 – 1100] kHz versus time. The numerous bursts in the IF frequency range occur with no clear pattern, and thus are ill-suited to forecast ELM activity.

Figure 15c: Integrated energy in the frequency band [1300 – 1700] kHz versus time. The precursor bursts are barely visible in the electron drift wave frequency band.